

DESIGN AND USES OF AN IRRADIANCE MONITORING
NETWORK FOR SHORT-TERM IRRADIANCE FORECASTING

by

Antonio Tomas Lorenzo

A Dissertation Submitted to the Faculty of the

COLLEGE OF OPTICAL SCIENCES

In Partial Fulfillment of the Requirements
For the Degree of

DOCTOR OF PHILOSOPHY

In the Graduate College

THE UNIVERSITY OF ARIZONA

This draft was generated on February 6, 2017.

THE UNIVERSITY OF ARIZONA
GRADUATE COLLEGE

As members of the Dissertation Committee, we certify that we have read the dissertation prepared by Antonio Tomas Lorenzo, titled Design and uses of an irradiance monitoring network for short-term irradiance forecasting and recommend that it be accepted as fulfilling the dissertation requirement for the Degree of Doctor of Philosophy.

Date: 14 April 2017

Alexander D. Cronin

Date: 14 April 2017

Matthias Morzfeld

Date: 14 April 2017

Barrett G. Potter Jr.

Final approval and acceptance of this dissertation is contingent upon the candidate's submission of the final copies of the dissertation to the Graduate College.

I hereby certify that I have read this dissertation prepared under my direction and recommend that it be accepted as fulfilling the dissertation requirement.

Date: 14 April 2017

Dissertation Director: Alexander D. Cronin

Date: 14 April 2017

Dissertation Director: Matthias Morzfeld

STATEMENT BY AUTHOR

This dissertation has been submitted in partial fulfillment of requirements for an advanced degree at the University of Arizona and is deposited in the University Library to be made available to borrowers under rules of the Library.

Brief quotations from this dissertation are allowable without special permission, provided that accurate acknowledgment of the source is made. Requests for permission for extended quotation from or reproduction of this manuscript in whole or in part may be granted by the head of the major department or the Dean of the Graduate College when in his or her judgment the proposed use of the material is in the interests of scholarship. In all other instances, however, permission must be obtained from the author.

SIGNED: Antonio Tomas Lorenzo

TABLE OF CONTENTS

LIST OF FIGURES	6
LIST OF TABLES	7
ABSTRACT	8
CHAPTER 1 INTRODUCTION	9
1.1 State of Solar Power in the Southwest	10
1.2 Solar Irradiance Forecasting	10
1.3 This Dissertation in Brief	10
CHAPTER 2 IRRADIANCE MONITORING NETWORK	12
2.1 Background	12
2.2 Design	12
2.3 Possible Improvements	12
CHAPTER 3 IRRADIANCE NETWORK FORECASTS	13
3.1 Irradiance Forecast Error Metrics	13
3.2 Future Work	13
CHAPTER 4 OPTIMAL INTERPOLATION TO IMPROVE SATELLITE NOWCASTS WITH DATA	14
4.1 Satellite to Irradiance Algorithms	14
4.2 Parameter Estimation	14
4.3 Future Work	14
CHAPTER 5 CONCLUSIONS	15
5.1 Future Work	15
APPENDIX A REPRINT: IRRADIANCE FORECASTS BASED ON AN IRRADIANCE MONITORING NETWORK, CLOUD MOTION, AND SPATIAL AVERAGING	16
APPENDIX B REPRINT: OPTIMAL INTERPOLATION OF SATELLITE AND GROUND DATA FOR IRRADIANCE NOWCASTING AT CITY SCALES	29

TABLE OF CONTENTS – *Continued*

APPENDIX C LIST OF PUBLICATIONS CO-AUTHORED BY A. T. LORENZO	39
REFERENCES	40

LIST OF FIGURES

Figure 1.1	Annual installations of solar PV in the US	9
Figure 1.2	Irradiance forecast errors across forecast horizons	11

LIST OF TABLES

ABSTRACT

write abstract as simple text here

CHAPTER 1

INTRODUCTION

The installed capacity of solar power in the US continues to grow as a result of aging coal and natural gas power plants, lower costs, state renewable portfolio standards, and efforts to decarbonize the electrical grid. As shown in Figure 1.1, this growth has been steady since 2010 and shows no signs of abating.

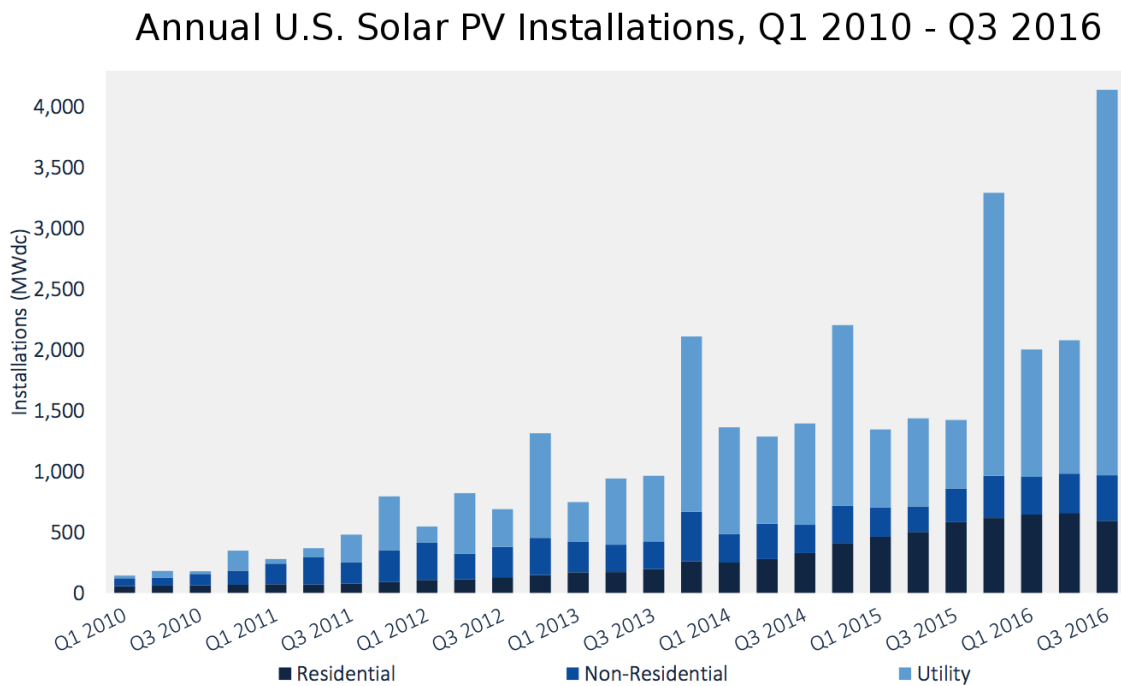


Figure 1.1: Annual installations of solar photovoltaic (PV) systems in the US.
[Source: [1]]

Solar irradiance is the fuel that drives all solar power plants. Unlike sources of fuel for conventional power generators like coal or natural gas, the solar resource is highly variable due to the nature of the chaotic system that is weather. This variability of the solar resource leads to uncertainty at the electric utility and increases

management costs [2]. Forecasts help utilities manage the variability in a number of ways [3, 4], including the optimal dispatch of battery storage [5].

This dissertation will explore solar irradiance forecasting at short time horizons (now to two hours in the future) made possible by an irradiance monitoring network. First, the current state of solar power in the Southwest US and a brief overview of forecasting methods will be discussed.

1.1 State of Solar Power in the Southwest

1.2 Solar Irradiance Forecasting

resource assessment short term wrf climatology

1.3 This Dissertation in Brief

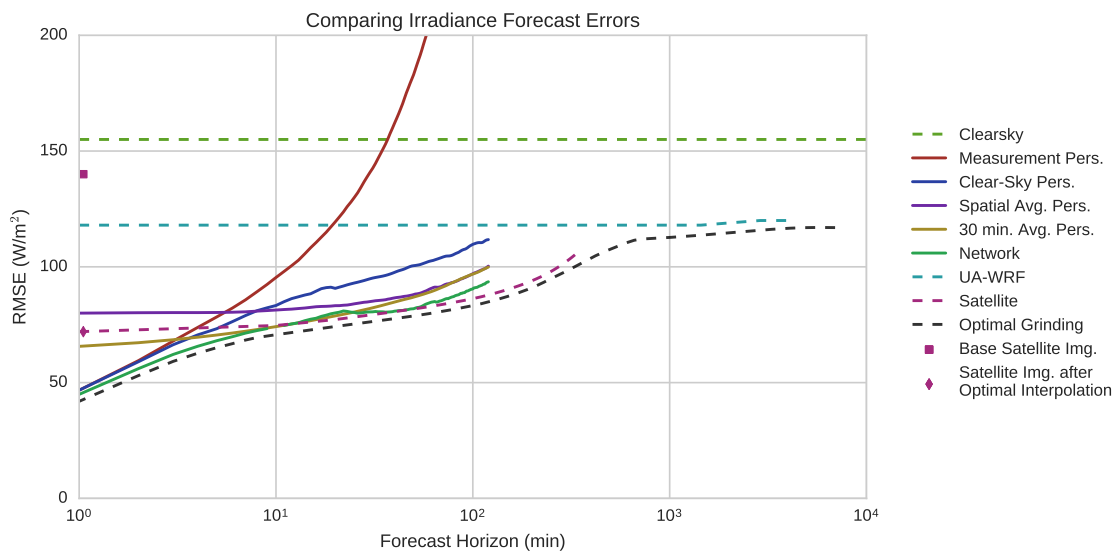


Figure 1.2: A comparison of irradiance forecast root-mean squared errors (RMSE) across many time horizons. The solid lines (and points) indicate forecasts that will be studied in depth in this dissertation. Dashed lines are based on preliminary analysis, but have not been studied in depth. Pers. refers to persistence, and UA-WRF refers to the numerical weather models generated at the UA using the Weather Research and Forecasting (WRF) model. The optimal grinding is a theoretical combination of forecasts at different time horizons for the best forecast at all horizons. The persistence and network forecasts will be discussed in Chapter 3 and the satellite image points will be discussed in Chapter 4.

CHAPTER 2

IRRADIANCE MONITORING NETWORK

2.1 Background

2.2 Design

2.3 Possible Improvements

CHAPTER 3

IRRADIANCE NETWORK FORECASTS

Background from vincent, how it's done, limitations, possible improvements

3.1 Irradiance Forecast Error Metrics

3.2 Future Work

CHAPTER 4

OPTIMAL INTERPOLATION TO IMPROVE SATELLITE NOWCASTS WITH DATA

- application - basic background - results - extension kalman filter etc
parameter estimation

4.1 Satellite to Irradiance Algorithms

4.2 Parameter Estimation

4.3 Future Work

Here is some future work

How does NSRDB do?

GSIP?

GOES-16

CHAPTER 5

CONCLUSIONS

5.1 Future Work

- blending horizons
 - wrf ensemble
 - probabilistic stuff

APPENDIX A

REPRINT: IRRADIANCE FORECASTS BASED ON AN IRRADIANCE
MONITORING NETWORK, CLOUD MOTION, AND SPATIAL AVERAGING

The following manuscript was published as a peer-reviewed article in Solar Energy. Further background material is presented in Chapter 3 of this dissertation. The manuscript is reprinted with permission from Elsevier. Original reference: A. T. Lorenzo, W. F. Holmgren, A. D. Cronin, 2015. Irradiance forecasts based on an irradiance monitoring network, cloud motion, and spatial averaging. Sol. Energy 122, 1158–1169. Copyright (2015) by Elsevier.



Available online at www.sciencedirect.com

ScienceDirect

Solar Energy 122 (2015) 1158–1169

**SOLAR
ENERGY**

www.elsevier.com/locate/solener

Irradiance forecasts based on an irradiance monitoring network, cloud motion, and spatial averaging

Antonio T. Lorenzo ^{a,*}, William F. Holmgren ^b, Alexander D. Cronin ^{c,a}^a University of Arizona, College of Optical Sciences, 1630 E. University Blvd., Tucson, AZ 85721, United States^b University of Arizona, Department of Atmospheric Sciences, 1118 E. 4th Street, Tucson, AZ 85721, United States^c University of Arizona, Department of Physics, 1118 E. 4th Street, Tucson, AZ 85721, United States

Received 2 July 2015; received in revised form 29 September 2015; accepted 10 October 2015

Communicated by: Associate Editor Jan Kleissl

Abstract

We describe and evaluate forecasts of solar irradiance using real-time measurements from a network of irradiance sensors. A forecast method using cloud motion vectors obtained from a numerical weather model shows significant skill over a standard persistence model for forecast horizons from 1 min to over 2 h, although the skill metric may be misleading. To explain this finding, we define and compare several different persistence methods, including persistence methods informed by an instantaneous spatial average of irradiance sensor output and persistence forecasts informed by a time-average of recent irradiance measurements. We show that spatial- or temporal-averaging reduces the forecast RMS errors primarily because these forecasts are smoother (have smaller variance). We use a Taylor diagram, which shows correlation, RMSE, and variance, to more accurately compare several different types of forecasts. Using this diagram, we show that forecasts using the network of sensors have meaningful skill up to 30 min time horizons after which the skill is primarily due to smoothing.

© 2015 Elsevier Ltd. All rights reserved.

Keywords: Solar forecasting; Solar irradiance; Sensor network

1. Introduction

The intermittency of solar power causes a cost to utilities and, ultimately, rate payers (Joskow, 2011). Solar power forecasts (Kleissl, 2013; Inman et al., 2013) may reduce these costs by enabling utilities to manage the variability of solar power in a number of ways. For example, forecasts can be used in conjunction with battery storage systems to control ramp-rates or provide frequency support (Hill et al., 2012; Cormode, 2015). Additionally, forecasts will provide utility grid operators with a prediction of

the expected photovoltaic (PV) output so they can more efficiently schedule backup generators.

A number of different techniques are used to forecast global horizontal irradiance (GHI). For forecast horizons in the intra-minute to a few minute range, techniques with input data from several ground sensors are often used (Achleitner et al., 2014; Elsinga and van Sark, 2014; Yang et al., 2015; Lipperheide et al., 2015).

For longer (intra-hour) forecast horizons, methods based on irradiance sensor networks (Lonij et al., 2013), machine learning techniques (Chu et al., 2015b), and sky imagers (Yang et al., 2014; Chu et al., 2015a) are being actively studied. Satellite image based forecasts are useful for 1-h to many hours in advance (Perez et al., 2010;

* Corresponding author.

E-mail address: atlorenzo@email.arizona.edu (A.T. Lorenzo).

Bilionis et al., 2014). For time horizons from several hours to up to a week in advance, numerical weather models often give the best predictions (Mathiesen and Kleissl, 2011; Diagne et al., 2014; Perez et al., 2013). Combinations of techniques are also being studied to extend the useful time horizon of a forecast (Marquez et al., 2013; Lauret et al., 2014).

Networks of irradiance sensors overcome some challenges typically associated with sky imagers or satellite images. For example, data from networks of irradiance sensors do not have the issue of converting pixel brightness to irradiance as sky imagers and satellite image methods have. Sky imagers and satellite images have the additional challenge of estimating cloud height to correctly project irradiance at cloud height to a location on the ground.

In this paper, we describe GHI forecasts that utilize a network of sensors placed throughout Tucson, AZ for April, May, and June 2014. The ideas behind this work are similar to those of Lonij et al. (2013), however the data sources and implementation are different. The rooftop PV network in Lonij et al. (2013) was limited to historical reports of 15 min average power, whereas the irradiance sensors used in the present research report 1 s resolution data with 1 min latency. This allows us to make higher resolution and, as we will see, more accurate forecasts.

We will show that our sensor network based forecasting method has significant skill when compared to a clear-sky index persistence forecast from 1 min to beyond 2 h time horizons. While the limited area and density of the network likely limits the skill and forecast horizon of our network-based forecasting method, the geographic diversity of measurements provide several advantages including improved persistence estimations. We will also explore why the forecasts exhibit such significant skill and explain this result is due to smoothing after 30 min forecast horizons.

First, we describe our network of irradiance sensors. Then, we describe how we use the network to make forecasts. A discussion of different types of persistence forecasts follows. Finally, we present and discuss our results and offer a concluding summary.

2. Irradiance sensor network forecasts

Our forecasting method relies on a network of sensors that sample the global horizontal irradiance at a number of locations. Our network consists of 12 irradiance sensors we developed, plus three rooftop PV power systems and one calibrated, commercial sensor. The calibrated sensor is part of a National Renewable Energy Laboratory (NREL) Solar Resource and Meteorological Assessment Project (SOLRMAP) site at the Univ. of Arizona (Wilcox and Andreas, 2010). Converting the data to clear-sky indices using an expected clear-sky profile for each sensor allows us to combine sensors that measure different quantities to make forecasts. These sensors are distributed throughout Tucson as shown in Fig. 1. The irradiance sensors we developed collect 1 s data and transmit

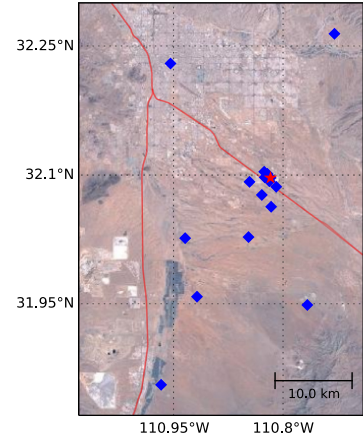


Fig. 1. Map of irradiance sensors used for this study in Tucson, AZ. The red star indicates the position of the sensor that was used to evaluate forecasts in Section 5. The sensor was chosen because of its proximity to 25 MW of installed PV power in and around the University of Arizona Science and Technology Park Solar Zone. The forecast area extends from 31.83° N to 32.28° N and 110.7° W to 111.15° W. (For interpretation of the references to color in this figure legend, the reader is referred to the web version of this article.)

it to a database every minute via cellular data networks (Lorenzo et al., 2014). Some use commercial pyranometers while others use photodiodes. Since we use clear-sky indices with data driven clear-sky profiles, the absolute error of the sensor is not a concern. However, the sensor used to evaluate the forecasted irradiance is a commercial sensor (Apogee SP-212) and agrees with the calibrated sensor to within 2% on average on clear days. The data were plotted for each day and for each sensor and verified by eye to provide some measure of quality control. See Lorenzo et al. (2015) for access to the dataset that was used in this study.

The first step in making our forecasts is to convert irradiance and PV power data to clear-sky index data. The clear-sky index for a sensor n at time t is defined as

$$k_n(t) = \frac{y_n(t)}{y_n^{clr}(t)}, \quad (1)$$

where $y_n(t)$ is the measured data and $y_n^{clr}(t)$ is the clear-sky expectation. Clear-sky expectations for each sensor are generated by fitting the measured data on a clear day in the recent past. An advantage of using this data-driven method of generating clear-sky expectations rather than a clear-sky model, such as the REST2 model (Guemard, 2008) or Ineichen model (Ineichen and Perez, 2002), is that the data-driven method inherently accounts for sensor orientation, permanent obstacles, and sensor calibration errors. Furthermore, because our forecasting method relies on forecasting clear-sky index and then converting back to

irradiance as a final step, the changes in atmospheric conditions between clear-sky days are not a major source of error in our final forecasts.

Next, we use the clear-sky indices to interpolate the scattered data onto a 1400 km^2 clear-sky index map for the Tucson region. To generate a clear-sky index map, we first create a 0.001° grid (with grid points approximately every 100 m) and add the sparse data from our network to the grid. We then set points along each boundary of the grid to the average of the clear-sky index values obtained from all the sensors. As we will see in Sections 4.4 and 5, this boundary condition helps to maintain forecast skill at longer time horizons.

Next, we fill all points in the grid with interpolated values as shown in Fig. 2. We chose to use multiquadric interpolation because it performs well at interpolating scattered geospatial data (Franke, 1982; Nuss and Titley, 1994), and it was more robust with our sparse data. We did not use a kriging method, even though kriging is often used to interpolate geospatial data, because we lack sufficient data to adequately estimate the variogram (Webster and Oliver, 1993; Sirayanone, 1988). We also explored inverse distance weighted interpolation, but found the output to be similar to multiquadric interpolation with insignificant differences in forecast errors (typically $<3 \text{ W/m}^2$ difference in the root mean square error for all forecast horizons).

Then, we translate this interpolated clear-sky map a distance determined by the cloud motion vectors (which may vary in time). The translation in the x direction, with the y translation being analogous, is given by

$$\Delta x(t_i, t) = \int_{t_i}^t v_x(t') dt', \quad (2)$$

where t_i is the time at which the forecast is being made, $t - t_i$ is the forecast horizon, and $v_x(t)$ is the x component of the time-varying cloud motion vector. Any grid points

that are missing data after the translation are filled with the average clear-sky index for all the sensors. Fig. 2 shows an example of an interpolated clear-sky index map and a map that has been shifted along the estimated cloud motion vector. Finally, we sample from this translated map at the desired forecast locations to obtain a forecasted clear-sky index which can be multiplied by the clear-sky expectation for that location to obtain an irradiance forecast. As we will discuss, for sufficiently long forecast horizons this procedure makes our network based forecasts indistinguishable from spatially-average persistence forecasts.

Forecasts out to 2 h in advance with 1 min time resolutions were made every 1 min for this analysis. As an example, one hour's worth of 5 min ahead forecasts along with measurements are shown in Fig. 3. This time-series is a composite showing snapshots (individual points) from 120 different forecasts that were each made 5 min in advance on a rolling basis. Concatenating points from different forecasts this way for several months lets us evaluate errors for forecasts with a 5 min horizon. Furthermore, updating forecasts every 1 min is valuable since 1 s data is constantly streaming into our database and each forecast has some new information that will likely improve the prediction for a specific time in the future. Later, we discuss errors as function of forecast horizon.

For estimating cloud motion velocity vector components (v_x, v_y), several techniques have been discussed including sensor correlations (Fung et al., 2014; Bosch et al., 2013), predictions from NWP (Lave and Kleissl, 2013; Lonij et al., 2013), analysis of aircraft communications addressing and reporting system (ACARS) or rawinsonde data, scaling of measured ground velocity, analysis of sky camera images (Urquhart et al., 2013), and analysis of satellite images (Hammer et al., 1999). For our analysis, we used modeled soundings (atmospheric temperature and

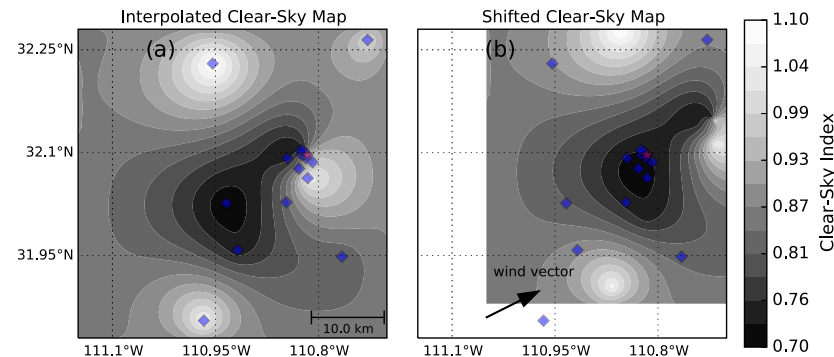


Fig. 2. An example interpolated map of clear-sky index on 5/19/14 near noon is shown in (a). Using the estimated cloud motion vectors this map is shifted according to desired forecast horizon as shown in (b). Then, samples from this shifted map are taken to as the forecasted clear-sky index for a particular location. The white space at bottom and left of (b) is filled in with the average clear-sky index of all sensors at the time the forecast is generated. The red star indicates the sensor that was used to evaluate forecasts. (For interpretation of the references to color in this figure legend, the reader is referred to the web version of this article.)

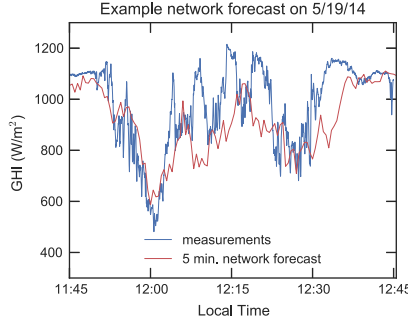


Fig. 3. An example of a 5 min ahead network forecast compared to measured data. Forecasts were generated every 1 min and the forecast for 5 min in the future is shown. The forecast and measurements at 12:00 show excellent agreement. For reference, the MAE for this entire period is 105 W/m^2 and the RMSE is 140 W/m^2 , and for 11:45 to 12:00 the MAE is 68 W/m^2 and the RMSE is 82 W/m^2 .

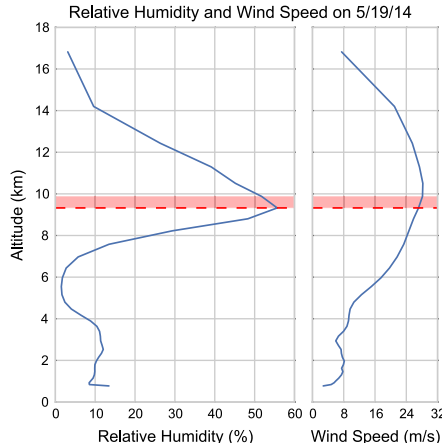


Fig. 4. Example vertical profiles of relative humidity and wind speed made by a numerical weather model on 5/19/14 at noon. To find the altitude at which clouds are most likely to form, we find the height with the greatest relative humidity (red dashed line). The winds at this height and heights within 90% of the maximum relative humidity (red shaded area) are averaged to produce an estimate of the cloud motion vector. (For interpretation of the references to color in this figure legend, the reader is referred to the web version of this article.)

dewpoint as a function of altitude/pressure) from the Weather Research and Forecasting (WRF) model run by the Univ. of Arizona, Dept. of Atmospheric Sciences (Leuthold, 2015). First, we compute a profile of relative humidity as a function of altitude averaged over the Tucson area from the WRF model. To estimate the cloud motion vectors, we find the altitude at which relative humidity is greatest (dashed line in Fig. 4), similar to Lave and Kleissl (2013). We then find all nearby heights

that have a relative humidity that is within 90% of the maximum (shaded area in Fig. 4). The wind speed and direction is then averaged for these altitudes and over the entire Tucson area to provide an estimated cloud motion vector. A new cloud motion vector is estimated in this way from each hourly output of the WRF model and then interpolated to 1 min time resolution. This simple estimation method has a number of limitations including only recognizing a single cloud layer and possibly selecting the wrong layer of the atmosphere i.e. one in which there are no clouds. This cloud motion estimation method along with the modest size and density of our network likely limits the overall accuracy of the network based forecasts presented here. Still, this network based method produces forecasts with lower errors than several standard persistence methods, as we discuss next.

3. Error metrics

We assessed the accuracy of forecasts using standard error metrics that are defined in Zhang et al. (2015). Each error metric is computed for forecast horizons, FH , ranging from 1 min to 30 min ($FH = 0, 1, \dots, 30$) by comparing forecasts, $y^{FH}(t_i)$, to subsequent instantaneous measurements, $y(t_i)$, of a single irradiance sensor. Errors were only computed when the solar zenith angle was less than 75° . Unless otherwise noted, only the 46 cloudy days in the study period were used to calculate error metrics and each metric is computed over this entire cloudy data set. Data and forecasts for a sensor (star in Fig. 1) in the middle of the network and near many large PV installations were used. Comparisons are always made with an instantaneous measurement, not averaged data, even when the forecast uses averaging.

In addition to root-mean squared error (RMSE) and mean absolute error (MAE), we also compute the centered root-mean squared error (CRMSE) for irradiance

$$\text{CRMSE}(FH) = \left(\frac{1}{N} \sum_{i=1}^N [(y^{FH}(t_i) - \bar{y}^{FH}) - (y(t_i) - \bar{y})]^2 \right)^{1/2}, \quad (3)$$

where an overbar indicates the sample mean of the quantity (Taylor, 2001). The CRMSE removes forecast bias and will become important later.

We also compute errors for forecasted clear-sky indices. This is valuable because, as opposed to irradiance, clear-sky index errors are not weighted based on the position of the sun in the sky.

We also define *relative* metrics in terms of clear-sky indices in order to present errors in percentages. The relative RMSE is

$$\text{rRMSE}(FH) = \bar{k}^{-1} \left(\frac{1}{N} \sum_{i=1}^N (k^{FH}(t_i) - k(t_i))^2 \right)^{1/2}. \quad (4)$$

Relative MAE is similarly defined as

$$\text{rMAE}(FH) = \bar{k}^{-1} \frac{1}{N} \sum_{i=1}^N |k^{FH}(t_i) - k(t_i)|. \quad (5)$$

Following the method of Marquez and Coimbra (2012), we can approximate forecast skill s as

$$s(FH) \approx 1 - \frac{\text{RMSE}(FH)}{\text{RMSE}_p(FH)}, \quad (6)$$

where RMSE_p is the RMSE for a clear-sky persistence forecast, described in Section 4.2. To estimate the average skill over many days, the ratio $\frac{\text{RMSE}}{\text{RMSE}_p}$ is estimated by the slope of the regression fit of daily RMSE vs RMSE_p . The average skill is then $\langle s \rangle = 1 - \text{slope}$. Examples of these plots and regressions are presented in Fig. 11.

4. Persistence forecasts

Persistence forecasts are the simplest type of forecast to implement and are often the most accurate at very short time horizons, making them a standard to compare with other methods. In this section we describe and compare the persistence forecasts we use for irradiance forecasting.

Before describing the various types of persistence, we first define the terminology we will use. The measured quantity of sensor n (e.g. irradiance) at time t will be denoted by $y_n(t)$. The forecast of sensor n at some time $t + FH$ in the future will be denoted by $y_n^*(t + FH)$. As mentioned in Section 3, we call FH the forecast horizon. The clear-sky expectation for a particular sensor will be denoted y_n^{clr} and the value of the clear-sky expectation at time t is $y_n^{clr}(t)$.

4.1. Measurement persistence

We call one of the simplest persistence methods “measurement persistence.” A measurement persistence forecast simply assumes that the irradiance at a future time will be the same as it is at the current time. Measurement persistence is defined by

$$y_n^*(t + FH) = y_n(t). \quad (7)$$

This type of persistence is useful for short time horizons, but it does not account for the diurnal cycle of irradiance due to changing solar position and this leads to large errors at longer time horizons as shown in Fig. 5.

4.2. Clear-sky index persistence

In this method, the clear-sky index is calculated at the current time and persisted into the future. A forecast of irradiance is obtained by multiplying this clear-sky index by the value of the clear-sky expectation at the forecast time. The equation for clear-sky index persistence is

$$y_n^*(t + FH) = \frac{y_n^{clr}(t + FH)}{y_n^{clr}(t)} \times y_n(t). \quad (8)$$

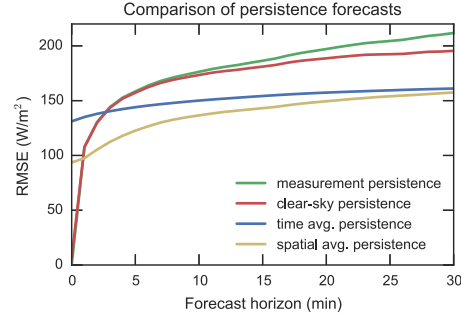


Fig. 5. Comparison of different types of persistence forecasts. RMSE, plotted as a function of forecast horizons, was computed for each type of forecast using data from the 46 cloudy days as described in Section 3. Spatially-averaged persistence has the lowest RMSE for all but the very shortest forecast horizons.

This method performs better than measurement persistence because it takes into account the diurnal cycle of irradiance, but it does require that a clear-sky expectation for the sensor, $y_n^{clr}(t)$, be known or modeled appropriately.

4.3. Time-averaged persistence

At time horizons greater than a few minutes, it can be beneficial to first average the measured clear-sky index over some time period defined by N time steps, each with period Δt , ending at some past time t_0 . This average clear-sky index is then multiplied by the clear-sky expectation of the target sensor to compute a forecast. Time-averaged persistence is thus computed as

$$y_n^*(t + FH) = y_n^{clr}(t + FH) \times \frac{1}{N} \sum_{i=0}^{N-1} \frac{y_n(t - t_0 - i\Delta t)}{y_n^{clr}(t - t_0 - i\Delta t)}. \quad (9)$$

Often, a rolling averaged is used so $t_0 = 0$, Δt is the time resolution of the measured data, and N is chosen so $(N - 1)\Delta t$ gives the desired averaging time. The total averaging time does not limit the frequency with which forecasts can be made. For example, a 5 min rolling average persistence can be recomputed every 1 min and still provide a useful forecast since new data is incorporated every time a forecast is made. An example of time-averaged persistence error with different averaging times using a rolling average is shown in Fig. 6.

4.4. Spatially-averaged persistence

If multiple measurements of irradiance are available in an area, one can make a persistence forecast based on the average clear-sky index of all the sensors. We refer to this method as spatially-averaged persistence. To make these forecasts, the measurements of multiple sensors are first converted to clear-sky indices using clear-sky expectations for each sensor. Then, these clear-sky indices are averaged

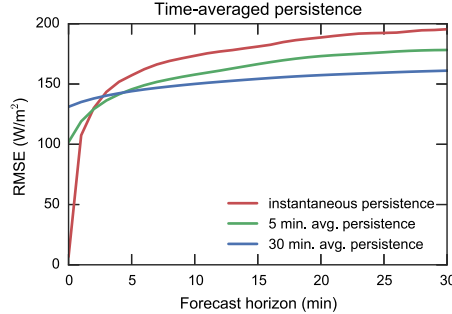


Fig. 6. Comparison of time-averaged persistence forecasts with different averaging times. The averages shown are made via a rolling average ($t_0 = 1$) with $\Delta t = 1$ s and N adjusted for each curve to give the appropriate total averaging time as described in Section 4.3. Longer time averages reduce errors at longer time horizons.

together. This average clear-sky index is then multiplied by the clear-sky expectation of the target sensor to produce a forecast for that sensor. Using N sensors, the spatially-averaged persistence for sensor n is

$$y_n^*(t + FH) = y_n^{clr}(t + FH) \times \frac{1}{N} \sum_{m=1}^N \frac{y_m(t)}{y_m^{clr}(t)}. \quad (10)$$

This method does not perform as well as clear-sky index persistence or measurement persistence at time horizons under a few minutes, as shown in Fig. 5, but it is more accurate (according the RMSE metric) than other persistence methods discussed here at longer (2–30 min) forecast horizons.

One could also imagine replacing the simple mean in Eq. (10) with a weighted mean by, for example, using the lasso (Yang et al., 2015) or some other shrinkage and selection method. Time and spatial averaging can also be combined as discussed in Section 5.1.

5. Results

We now present the results of the network and persistence forecasts using metrics defined in Zhang et al. (2015) and Section 3 for the study period of April, May, and June 2014. First, we evaluate persistence forecasts. Then, we study network forecast errors in depth. Finally, we compare network forecasts to other irradiance forecasting methods.

5.1. Persistence forecast results

Root-mean squared errors from the four types of persistence forecasts described above are plotted in Fig. 5. We see that for the 46 cloudy days we studied in Tucson, AZ., the two types of input averaging, spatial and temporal, both improve forecasts compared to clear-sky index persistence after time horizons of a few minutes. The cross-

over time depends on the weather. As expected, clear-sky index persistence performs better than measurement persistence because it accounts for the diurnal cycle.

Though Fig. 5 shows spatially-averaged persistence outperforming time-averaged persistence, the averaging time and number of sensors averaged can change these curves significantly. Figs. 6 and 7 show various averaging times and number of sensors in the average, respectively. We see that longer averaging times reduce errors at time horizons greater than 5 min but are worse at shorter time horizons. The common auto-regressive moving average (ARMA) model similarly weights previous values and/or errors to produce a forecast. We also see that adding more sensors to a spatially-averaged persistence reduces errors except at time horizons shorter than a few minutes.

One explanation for our finding that spatially-averaged persistence performs better than time-averaged persistence is related to the number of dimensions in each average. Using kinematics ($x = vt$) we can map the time series $y_i(t)$ onto a one-dimensional transect in space downwind from the sensor. In comparison, the spatial average uses data from locations that are distributed in two dimensions including some locations that are upwind of the location of interest. By averaging over two dimensions, not one, spatial average persistence effectively uses more independent samples of the cloud field. This theory assumes that all sensors are subject to the same cloud field, which is reasonable for the size of our network.

When we average the input data over both space and time, as shown as the green line in Fig. 8, we find the RMSE is lower at longer time horizons.

5.2. Network forecast results

We now compare our network forecasts to a clear sky ($k_n^*(t) = 1$) forecast, measurement persistence, clear-sky index persistence, and spatially averaged persistence (using the same 16 sensors which were used to make the network forecast). Fig. 9 shows the MAE for these methods for only

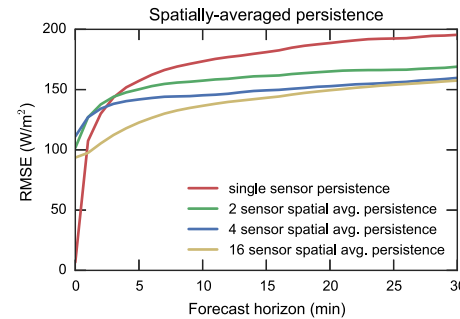


Fig. 7. Comparison of spatially-average persistence forecasts with a varying number of sensors averaged. Adding more sensors to the spatial average improves the forecast RMSE.

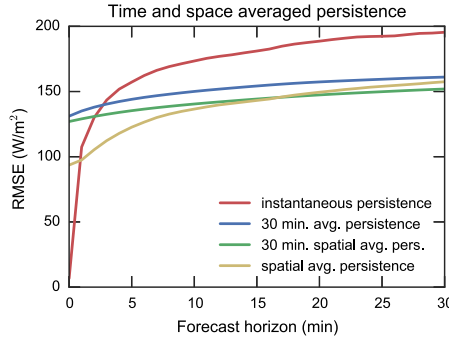


Fig. 8. Comparison of a persistence forecast made by first averaging over space and then averaging over time (green line) to other persistence methods. Averaging in time and space marginally improves forecasts at longer time horizons. (For interpretation of the references to color in this figure legend, the reader is referred to the web version of this article.)

cloudy days while Fig. 10 shows the RMSE. Plots of CRMSE show similar trends. Note that network forecasts have nonzero error at zero forecast horizons because of the smoothing applied when making the interpolated clear-sky index map and due to limiting the maximum forecasted clear-sky index to 1.25. We see that network forecasts have lower MAE than other methods for time horizons from 1 min to 30 min. We only graph up to 30 min forecast horizons because the 30 min to 2 h errors are similar and uninteresting. Fig. 10 shows that the network forecasts have lower RMS errors than the other methods at forecast horizons less than about 4 min and then have slightly higher RMSE values than spatially-averaged persistence. This difference between RMSE and MAE suggests that network forecasts have fewer small errors but more large errors than spatially-averaged persistence forecasts. For completeness, we also present error metrics for all 91 days in the study period in Appendix A. Clear days show similar trends

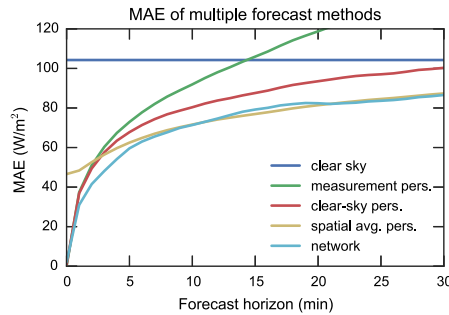


Fig. 9. MAE of many types of forecasts averaged over 46 cloudy days. Clear sky refers to a forecast where one assumes the sky is always clear ($k_n^*(t) = 1$). Network forecasts have the lowest MAE at all time horizons shown.

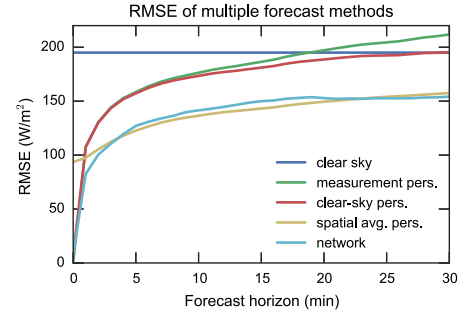


Fig. 10. RMSE of many types of forecasts averaged over 46 cloudy days. Clear sky refers to a forecast where one assumes the sky is always clear ($k_n^*(t) = 1$).

but with smaller errors which lowers the 91 day average RMSE by 40–50% depending on the time horizon.

We also compute forecast skill as defined by Marquez and Coimbra (2012). Fig. 11 illustrates the regressions used to calculate the average skill of our forecasts. At low clear-sky index persistence RMSE values (e.g. clear days), we see that the skill is negative (network RMSE > clear-sky index persistence RMSE). For days with larger clear-sky index persistence RMSE values, we see that our network forecasts have positive skill. The average skill found from regressions, typically 20%, is plotted in Fig. 12 as a function of forecast horizon.

5.3. Exploration of forecast errors

The forecast skill of the network-based forecasts remains at a surprising +20% at time horizons through 2 h. This was unexpected because the finite domain of the network is usually transited by clouds in 10–20 min. To explain this finding, we revisited the underlying statistics of forecast skill. The root mean squared error can be written as

$$\text{RMSE} = \sqrt{\sigma_f^2 + \sigma_o^2 - 2\sigma_f\sigma_o\rho + \text{MBE}^2}, \quad (11)$$

where σ_f is the forecast standard deviation, σ_o is the measurement standard deviation, ρ is the correlation coefficient, and MBE is the mean bias error (Taylor, 2001). When correlations and biases are small, the RMSE reduces to a sum in quadrature of the observation and measurement standard deviations. Under these conditions, a smoother forecast will have a lower RMSE, and thus a more positive forecast skill, than a more variable forecast. Of course, this does not mean that the smoother forecast is more skillful under most definitions of the word.

As an alternative means of understanding the relative merits of our forecast methods, we turned to Taylor diagrams (Taylor, 2001). The Taylor diagram in Fig. 13 shows the CRMSE, correlation coefficient, and standard

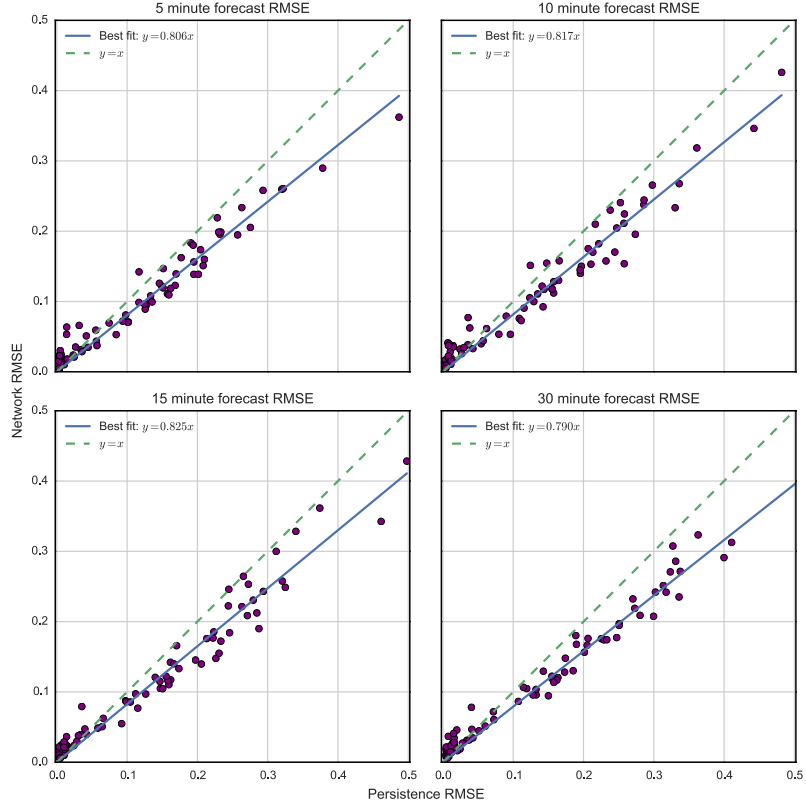


Fig. 11. Network RMSE vs clear-sky index persistence RMSE for all days and 5, 10, 15, and 30 min forecast horizons calculated for clear-sky indices. The slope of the best fit line is used to approximate the skill of the forecasts. Each point represents one day of data and forecasts. The forecast skill is positive for any point below the $y = x$ line. The plots illustrate that network forecasts may have negative skill for days that are nearly clear. Furthermore, they show a consistent positive skill for cloudier days with few outliers.

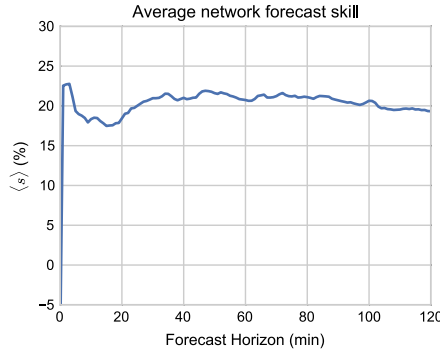


Fig. 12. Average skill of our network forecasts for the study period of April, May, and June 2014.

deviations of clear-sky index forecasts for each forecast method. Here, we analyzed forecasts of clear-sky index instead of irradiance so all values are dimensionless. The solid contour lines are lines of constant CRMSE. We see that network forecasts have correlations greater than or approximately equal to spatially-averaged persistence but with higher standard deviation. This means network forecasts capture more variability. Network forecast standard deviation transitions from performing like clear-sky index persistence forecasts at short time horizons to approaching spatially-averaged persistence, analogous to the transitions for MAE and RMSE in Figs. 9 and 10. At roughly 30 min forecast horizons, network forecasts behave about the same as spatially-averaged persistence forecasts as we expect based on the method used and average cloud velocities. Hence, we say that our network forecasts are more useful than simple spatial averaging for forecast horizons

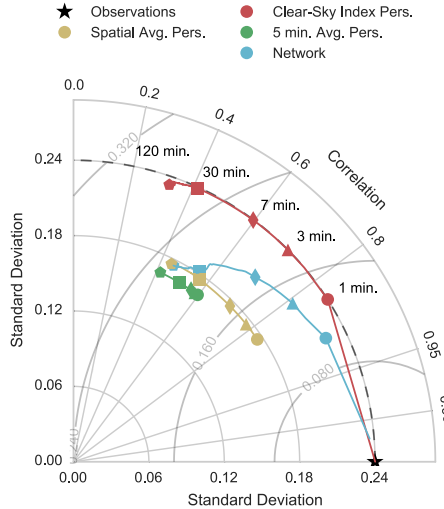


Fig. 13. Taylor diagram for clear-sky index persistence (red), spatially-averaged persistence (yellow), 5-min time-averaged persistence (green), and network (light blue) forecasts for 1 min (circle), 3 min (triangle), 7 min (diamond), 30 min (square), and 120 min (pentagon) forecast horizons. The black dashed line indicates the standard deviation of the data. Solid contours around the observations point are lines of constant CRMSE. Forecasts for clear-sky index were used so all quantities are dimensionless. At the 120 min forecast horizon, the spatially-averaged persistence and network points overlap. Network forecasts start with a standard deviation near that of the measurements, but this decreases at longer time horizons as the network forecast begins to resemble spatially-averaged persistence. (For interpretation of the references to color in this figure legend, the reader is referred to the web version of this article.)

less than 30 min. Regardless of their forecast skill metric scores, assessing the utility of network and spatial-average persistence forecasts past 30 min is challenging. We therefore suggest that researchers restrict their use of forecast skill to methods which have similar mean bias errors and standard deviations.

Fig. 13 also shows how network and spatially-averaged persistence forecasts always have lower RMSE than clear-sky index persistence after a certain horizon. This is a result of the combination of lower standard deviation and higher correlation for the network and spatially-averaged persistence forecasts. This trend holds for even longer forecast horizons. Unfortunately, Eq. (11) does not simplify for the forecasts and data shown here so both correlation and standard deviation need to be considered to understand RMSE.

5.4. Limitations and comparisons to other work

One limitation of the current network algorithm is that it does not account for multiple cloud layers. Satellite images from many of the studied days confirm that multiple cloud layers were moving in different directions. We

also studied incorporating data from times in the past appropriately shifted by cloud motion vectors but found no noticeable improvement, likely due to this complex motion.

On a day with a single cloud layer coming from the southwest shown in Fig. 14, we see that a single upstream sensor greatly improves network forecasts at around the 7 min forecast horizon. This demonstrates that the network method can perform quite well if the velocity of the clouds is well defined and the sensors are appropriately located.

Another limitation is the size of the irradiance network. Depending on the wind motion vectors clouds can pass from the edge of the network to the center in 10 min. Since the boundary is set to the spatial average of sensors, network forecasts converge to spatially averaged persistence.

Still, our current method of network forecasting performs as well as or better than both clear-sky index and spatially-averaged persistence. Error statistics for network forecasts for cloudy days are presented in Table 1.

When we compared our current network method and high resolution data with the previous work of Lonij et al. (2013), we see that our new method performs favorably. Lonij et al. use a network of 80 rooftop PV systems in the Tucson area with 15 min averaged power data to make short-term forecasts of power. Their method uses a similar cloud translation method as this work, but wind vectors are obtained from NOAA forecasts, via optimization of the wind vector to minimize RMS forecast errors, or via a Kalman filter applied to optimized vectors. At 15 and 30 min forecast horizons, the best forecasts of Lonij et al. had skills of -8.0% and 2.4%, respectively, while our new method has skills of 17.7% and 21.2%. Even compared to the optimized “forecasts” (which were not true forecasts) with skills of 1.6% and 34.5% at 15 and

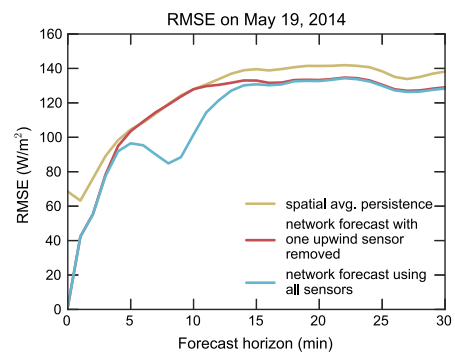


Fig. 14. RMSE vs forecast horizon on May 19, 2014 for network forecasts made with all the sensors in the network (blue) and with one upwind sensor removed (red), along with a spatially-averaged persistence forecast (yellow). The dip at 7 min for the forecast using the full network illustrates that properly placed upstream sensors do improve forecasts over a simple spatial average. (For interpretation of the references to color in this figure legend, the reader is referred to the web version of this article.)

Table 1

Summary of error statistics for network forecasts for the 46 days with clouds. Error statistics were calculated for the entire dataset at once. Only forecasts and data with solar zenith angle less than 75° were used. The mean irradiance was $\bar{y} = 662 \text{ W/m}^2$ and the mean clear-sky index was $k = 0.92$.

FH (min)	rMAE (%)	MAE (W/m^2)	MBE (W/m^2)	rRMSE (%)	RMSE (W/m^2)	Avg. skill (%)
1	4.96	30.97	-1.44	11.90	82.55	22.96
3	7.51	48.13	-1.39	15.89	110.46	23.09
5	9.29	59.59	-3.91	18.67	127.06	19.65
10	11.39	71.38	-8.59	22.11	141.44	18.63
20	13.23	82.39	-10.46	24.03	152.84	18.66
30	13.95	86.57	-7.52	24.49	154.15	21.21
60	15.45	95.59	-6.65	26.59	160.72	21.00
120	17.02	106.51	-2.01	29.20	172.45	19.58

30 min, our new method performs well. We only used 3 months of data from our real-time network while Lonij et al. used one year of data.

Chu et al. (2015b) produced a cloud tracking forecast of PV power with an ANN applied to a deterministic forecast using a sky imager at a site near the Nevada/Arizona border. The initial deterministic forecast model does not perform well compared to persistence, with negative skills at 5, 10, and 15 min forecast horizons. However, the reforecast using an ANN technique improves the result with skills of 15.1%, 21.8%, and 26.2% at forecast horizons of 5, 10, and 15 min respectively, which are comparable to our technique. Similar optimization could be applied to our deterministic network forecasts to further improve skill. A Taylor diagram of both the initial deterministic forecast and ANN re-forecast would be useful as another method to assess the forecasts.

Compared to the regression methods in Yang et al. (2015), our forecasts perform comparably at the 5 min forecast horizon. Yang et al. used 1 s irradiance data from Oahu and applied the lasso and ordinary least squares regression methods to make very short term (< 5 min) forecasts. At shorter horizons, both methods can outperform the reference persistence forecast. Since our forecasts approach the clear-sky index persistence model, regression methods are likely a better choice if sub-five minute time horizons forecasts are needed, at least for the region studied here.

6. Conclusion

We presented a deterministic method to forecast irradiance that uses data from a network of irradiance sensors as the primary input. This method can combine the benefits of clear-sky index persistence and spatially-averaged persistence into one forecast. It outperforms a reference clear-sky index persistence model for 1–120 min forecast horizons. Much of this improvement is due to spatial averaging, which shows surprising utility for the region and time period studied. However, network forecasts still exhibit more variability than spatially-averaged persistence, thus we claim network forecasts are better at forecasts horizons less than 30 min. The results presented here used numerical weather model winds at a single layer of the

atmosphere to perform cloud advection, so complex cloud movement or incorrect cloud motion vectors likely limited the accuracy. The limited size and density of the network also limits the accuracy of network forecasts.

We showed that forecast skill can be a misleading metric, and we instead used a Taylor diagram to better understand the differences among forecast methods. This lead us to reinterpret our finding that network forecasts show significant skill to 2 h forecast horizons so now we make a more informed claim that network forecasts show meaningful skill out to 30 min forecast horizons. We encourage other authors to make use of Taylor diagrams when assessing the quality of forecasts.

While the method presented may have a limited useful maximum forecast horizon, the irradiance sensor network will be a valuable asset to make other types of forecasts. For instance, regression methods using a network can improve very short time horizon forecasts (Yang et al., 2015). In the future, we could use the network of sensors to improve satellite image forecasts similar to Marquez et al. (2013) and to validate numerical weather model forecasts. We may also study how different interpolation methods affect the results of our network-based forecasting method in a detailed comparison.

Acknowledgments

This work was supported by Tucson Electric Power (TEP). We thank Mike Leuthold from the University of Arizona Department of Atmospheric Sciences for providing WRF data, and the University of Arizona Renewable Energy Network (UAREN) for institutional support. We also thank Technicians for Sustainability, a local solar PV installer, for providing data from rooftop PV systems in near real-time for forecasting and analysis. WFH thanks the Department of Energy (DOE) Office of Energy Efficiency and Renewable Energy (EERE) Postdoctoral Research Award for support.

Appendix A. Analysis for both clear and cloudy days

Table A.2 presents error statistics calculated over all 91 days in the study period. As expected, the magnitude of errors is smaller when more clear days are included.

Table A.2

Summary of error statistics for network forecasts for all 91 days. Error statistics were calculated for the entire dataset at once. Only forecasts and data with solar zenith angle less than 75° were used. The mean irradiance was $\bar{y} = 694 \text{ W/m}^2$ and the mean clear-sky index was $\bar{k} = 0.96$.

FH (min)	rMAE (%)	MAE (W/m^2)	MBE (W/m^2)	rRMSE (%)	RMSE (W/m^2)	Avg. skill (%)
1	2.92	18.40	-0.97	8.84	61.67	22.54
3	4.40	28.31	-1.69	11.71	81.31	22.77
5	5.43	35.09	-4.05	13.70	93.09	19.36
10	6.76	42.90	-8.48	16.19	103.53	18.33
20	7.78	49.06	-9.79	17.58	111.76	18.43
30	8.16	51.35	-8.43	17.91	112.73	20.97
60	8.97	56.41	-7.88	19.44	117.55	20.74
120	9.89	62.72	-4.75	21.34	126.16	19.33

Appendix B. Supplementary material

Location metadata, measurements, clear-sky expectations, and cloud motion vectors used in this study have been released online under the CC-BY-NC 4.0 license (Lorenzo et al., 2015).

References

- Achleitner, S., Kamthe, A., Liu, T., Cerpa, A.E., 2014. SIPS: solar irradiance prediction system. In: IPSN-14 Proceedings of the 13th International Symposium on Information Processing in Sensor Networks, pp. 225–236. <http://dx.doi.org/10.1109/IPSN.2014.6846755>.
- Bilionis, I., Constantinescu, E.M., Anitescu, M., 2014. Data-driven model for solar irradiation based on satellite observations. Sol. Energy 110, 22–38. <http://dx.doi.org/10.1016/j.solener.2014.09.009>.
- Bosch, J., Zheng, Y., Kleissl, J., 2013. Deriving cloud velocity from an array of solar radiation measurements. Sol. Energy 87, 196–203. <http://dx.doi.org/10.1016/j.solener.2012.10.020>.
- Chu, Y., Pedro, H.T., Li, M., Coimbra, C.F., 2015a. Real-time forecasting of solar irradiance ramps with smart image processing. Sol. Energy 114, 91–104. <http://dx.doi.org/10.1016/j.solener.2015.01.024>.
- Chu, Y., Urquhart, B., Gohari, S.M., Pedro, H.T., Kleissl, J., Coimbra, C. F., 2015b. Short-term reforecasting of power output from a 48 MW solar PV plant. Sol. Energy 112, 68–77. <http://dx.doi.org/10.1016/j.solener.2014.11.017>.
- Cormode, D., 2015. Large and Small Photovoltaic Powerplants. Phd Dissertation. University of Arizona.
- Diagne, M., David, M., Boland, J., Schmutz, N., Lauret, P., 2014. Post-processing of solar irradiance forecasts from WRF model at Reunion Island. Sol. Energy 105, 99–108. <http://dx.doi.org/10.1016/j.solener.2014.03.016>.
- Elsinga, B., van Sark, W.G., 2014. Inter-system time lag due to clouds in an urban PV ensemble. In: 2014 IEEE 40th Photovoltaic Specialist Conference (PVSC). No. 4, pp. 0754–0758. <http://dx.doi.org/10.1109/PVSC.2014.6925029>.
- Franke, R., 1982. Scattered data interpolation: tests of some methods. Math. Comput. 38 (157), 181–200. <http://dx.doi.org/10.1090/S0025-5718-1982-0637296-4>.
- Fung, V., Bosch, J.L., Roberts, S.W., Kleissl, J., 2014. Cloud shadow speed sensor. Atmos. Meas. Tech. 7 (6), 1693–1700. <http://dx.doi.org/10.5194/amt-7-1693-2014>.
- Guemard, C.A., 2008. REST2: high-performance solar radiation model for cloudless-sky irradiance, illuminance, and photosynthetically active radiation validation with a benchmark dataset. Sol. Energy 82 (3), 272–285. <http://dx.doi.org/10.1016/j.solener.2007.04.008>.
- Hammer, A., Heinemann, D., Lorenz, E., Lückebe, B., 1999. Short-term forecasting of solar radiation: a statistical approach using satellite data. Sol. Energy 67 (1–3), 139–150. [http://dx.doi.org/10.1016/S0038-092X\(00\)00038-4](http://dx.doi.org/10.1016/S0038-092X(00)00038-4).
- Hill, C.A., Such, M.C., Chen, D., Gonzalez, J., Grady, W.M., 2012. Battery energy storage for enabling integration of distributed solar power generation. IEEE Trans. Smart Grid 3 (2), 850–857. <http://dx.doi.org/10.1109/TSG.2012.2190113>.
- Ineichen, P., Perez, R., 2002. A new airmass independent formulation for the Linke turbidity coefficient. Sol. Energy 73 (3), 151–157. [http://dx.doi.org/10.1016/S0038-092X\(02\)00045-2](http://dx.doi.org/10.1016/S0038-092X(02)00045-2).
- Iman, R.H., Pedro, H.T., Coimbra, C.F., 2013. Solar forecasting methods for renewable energy integration. Prog. Energy Combust. Sci. 39 (6), 535–576. <http://dx.doi.org/10.1016/j.pecs.2013.06.002>.
- Joskow, P.L., 2011. Comparing the costs of intermittent and dispatchable electricity generating technologies. Am. Econ. Rev. 101 (3), 238–241. <http://dx.doi.org/10.1257/aer.101.3.238>.
- Kleissl, J. (Ed.), 2013. Solar Energy Forecasting and Resource Assessment, first ed. Elsevier, Oxford. <http://dx.doi.org/10.1016/B978-0-12-397177-7.18001-5>.
- Lauret, P., Diagne, M., David, M., 2014. A neural network post-processing approach to improving NWP solar radiation forecasts. Energy Procedia 57, 1044–1052. <http://dx.doi.org/10.1016/j.egypro.2014.10.089>.
- Lave, M., Kleissl, J., 2013. Cloud speed impact on solar variability scaling application to the wavelet variability model. Sol. Energy 91, 11–21. <http://dx.doi.org/10.1016/j.solener.2013.01.023>.
- Leuthold, M., 2015. The University of Arizona Department of Atmospheric Sciences – Arizona Regional WRF Model Data. <<http://www.atmo.arizona.edu/index.php?section=weather&id=wrf>>.
- Lipperheide, M., Bosch, J., Kleissl, J., 2015. Embedded nowcasting method using cloud speed persistence for a photovoltaic power plant. Sol. Energy 112, 223–238. <http://dx.doi.org/10.1016/j.solener.2014.11.013>.
- Lonij, V.P., Brooks, A.E., Cronin, A.D., Leuthold, M., Koch, K., 2013. Intra-hour forecasts of solar power production using measurements from a network of irradiance sensors. Sol. Energy 97, 58–66. <http://dx.doi.org/10.1016/j.solener.2013.08.002>.
- Lorenzo, A.T., Cronin, A.D., Holmgren, W.F., 2015. Irradiance Monitoring Network Data and Wind Motion Vectors. <<http://zenodo.org/record/29070>>.
- Lorenzo, A.T., Holmgren, W.F., Leuthold, M., Kim, C.K., Cronin, A.D., Betterton, E.A., 2014. Short-term PV power forecasts based on a real-time irradiance monitoring network. 2014 IEEE 40th Photovoltaic Specialist Conference (PVSC), pp. 0075–0079. <http://dx.doi.org/10.1109/PVSC.2014.6925212>.
- Marquez, R., Coimbra, C.F.M., 2012. Proposed metric for evaluation of solar forecasting models. J. Sol. Energy Eng. 135 (1), 011016. <http://dx.doi.org/10.1115/1.4007496>.
- Marquez, R., Pedro, H.T., Coimbra, C.F., 2013. Hybrid solar forecasting method uses satellite imaging and ground telemetry as inputs to ANNs. Sol. Energy 92, 176–188. <http://dx.doi.org/10.1016/j.solener.2013.02.023>.
- Mathiesen, P., Kleissl, J., 2011. Evaluation of numerical weather prediction for intra-day solar forecasting in the continental United States. Sol. Energy 85 (5), 967–977. <http://dx.doi.org/10.1016/j.solener.2011.02.013>.

- Nuss, W.A., Titley, D.W., 1994. Use of multiquadric interpolation for meteorological objective analysis. *Mon. Weather Rev.* 122 (7), 1611–1631. [http://dx.doi.org/10.1175/1520-0493\(1994\)122<1611:UOMIFM>2.0.CO;2](http://dx.doi.org/10.1175/1520-0493(1994)122<1611:UOMIFM>2.0.CO;2).
- Perez, R., Kivalov, S., Schlemmer, J., Hemker, K., Renné, D., Hoff, T.E., 2010. Validation of short and medium term operational solar radiation forecasts in the US. *Sol. Energy* 84 (12), 2161–2172. <http://dx.doi.org/10.1016/j.solener.2010.08.014>.
- Perez, R., Lorenz, E., Pelland, S., Beauharnois, M., Van Knowe, G., Hemker, K., Heinemann, D., Remund, J., Müller, S.C., Traunmüller, W., Steinmauer, G., Pozo, D., Ruiz-Arias, J.A., Lara-Fanego, V., Ramirez-Santigosa, L., Gaston-Romero, M., Pomares, L.M., 2013. Comparison of numerical weather prediction solar irradiance forecasts in the US, Canada and Europe. *Sol. Energy* 94, 305–326. <http://dx.doi.org/10.1016/j.solener.2013.05.005>.
- Sirayanone, S., 1988. Comparative Studies of Kriging, Multiquadric-Biharmonic and other Methods for Solving Resources Problems. Dissertation. Iowa State University.
- Taylor, K.E., 2001. Summarizing multiple aspects of model performance in a single diagram. *J. Geophys. Res.: Atmos.* 106 (D7), 7183–7192. <http://dx.doi.org/10.1029/2000JD900719>.
- Urquhart, B., Ghonima, M., Nguyen, D.A., Kurtz, B., Chow, C.W., Kleissl, J., 2013. Sky-imaging systems for short-term forecasting. *Solar Energy Forecasting and Resource Assessment*. Elsevier, pp. 195–232. <http://dx.doi.org/10.1016/B978-0-12-397177-7.00009-7> (Chapter 9).
- Webster, R., Oliver, M.A., 1993. How large a sample is needed to estimate the regional variogram adequately? In: Soares, A. (Ed.), *Geostatistics Tróia 92 SE – 14*. In: Quantitative Geology and Geostatistics, vol. 5. Springer, Netherlands, pp. 155–166. http://dx.doi.org/10.1007/978-94-011-1739-5_14.
- Wilcox, S., Andreas, A., 2010. Solar Resource & Meteorological Assessment Project (SOLRMAP): Observed Atmospheric and Solar Information System (OASIS); Tucson, Arizona (Data). <http://dx.doi.org/10.7799/105226>.
- Yang, D., Ye, Z., Lim, L.H. I., Dong, Z., 2015. Very short term irradiance forecasting using the lasso. *Sol. Energy* 114, 314–326. <http://dx.doi.org/10.1016/j.solener.2015.01.016>.
- Yang, H., Kurtz, B., Nguyen, D., Urquhart, B., Chow, C.W., Ghonima, M., Kleissl, J., 2014. Solar irradiance forecasting using a ground-based sky imager developed at UC San Diego. *Sol. Energy* 103, 502–524. <http://dx.doi.org/10.1016/j.solener.2014.02.044>.
- Zhang, J., Florita, A., Hodge, B.-M., Lu, S., Hamann, H.F., Banunarayanan, V., Brockway, A.M., 2015. A suite of metrics for assessing the performance of solar power forecasting. *Sol. Energy* 111, 157–175. <http://dx.doi.org/10.1016/j.solener.2014.10.016>.

APPENDIX B

REPRINT: OPTIMAL INTERPOLATION OF SATELLITE AND GROUND
DATA FOR IRRADIANCE NOWCASTING AT CITY SCALES

The following manuscript was published as a peer-reviewed article in Solar Energy. Further discussion of this article is presented in Chapter 4 of this dissertation. The manuscript is reprinted with permission from Elsevier. Original reference: A. T. Lorenzo, M. Morzfeld, W. F. Holmgren, A. D. Cronin, 2017. Optimal interpolation of satellite and ground data for irradiance nowcasting at city scales. Sol. Energy 144, 466–474. Copyright (2017) by Elsevier.



Optimal interpolation of satellite and ground data for irradiance nowcasting at city scales



Antonio T. Lorenzo ^{a,*}, Matthias Morzfeld ^b, William F. Holmgren ^c, Alexander D. Cronin ^{d,a}

^a University of Arizona, College of Optical Sciences, 1630 E. University Blvd., Tucson, AZ 85721, United States

^b University of Arizona, Department of Mathematics, 617 N. Santa Rita Ave., Tucson, AZ 85721, United States

^c University of Arizona, Department of Hydrology & Atmospheric Sciences, 1118 E. 4th Street, Tucson, AZ 85721, United States

^d University of Arizona, Department of Physics, 1118 E. 4th Street, Tucson, AZ 85721, United States

ARTICLE INFO

Article history:

Received 16 November 2016

Received in revised form 4 January 2017

Accepted 15 January 2017

Keywords:

Solar irradiance

Optimal interpolation

Data assimilation

Nowcasting

ABSTRACT

We use a Bayesian method, optimal interpolation, to improve satellite derived irradiance estimates at city-scales using ground sensor data. Optimal interpolation requires error covariances in the satellite estimates and ground data, which define how information from the sensor locations is distributed across a large area. We describe three methods to choose such covariances, including a covariance parameterization that depends on the relative cloudiness between locations. Results are computed with ground data from 22 sensors over a 75×80 km area centered on Tucson, AZ, using two satellite derived irradiance models. The improvements in standard error metrics for both satellite models indicate that our approach is applicable to additional satellite derived irradiance models. We also show that optimal interpolation can nearly eliminate mean bias error and improve the root mean squared error by 50%.

© 2017 Elsevier Ltd. All rights reserved.

1. Introduction

Estimates of global horizontal irradiance (GHI) are essential at many stages of photovoltaic (PV) system deployment and operation. A widely used technique is to compute GHI from geostationary satellite images, which are typically available every 15–30 min and cover large areas of the globe. Such satellite derived estimates of GHI are commonly used to design and site PV power plants (Vignola et al., 2013), to forecast the output of a fleet of PV generators (Kühnert et al., 2013), and to provide real-time estimates of distributed generation (DG) or “behind the meter” generation of rooftop PV systems (Saint-Drenan et al., 2011). Satellite derived estimates have also been used to detect failures in PV systems (Drews et al., 2007).

In addition to satellite derived GHI estimates, one may have access to ground sensors that provide more accurate GHI measurements, but are often sparsely distributed. We present a method that combines the broad areal coverage of satellite derived GHI with the accurate point measurements from ground sensors in order to provide more accurate GHI estimates for city-scale areas.

Similar techniques have used ground measurements to improve satellite derived irradiance estimates in the context of improving daily (or longer) irradiance estimates. Much of this work studies

so called site adaptation techniques with the goal of improving multi-year satellite irradiance estimates using a limited measurement campaign from ground sensors (Polo et al., 2016). A number of studies use Kriging methods that rely on spatial interpolation of the ground data along with satellite derived estimates (D'Agostino and Zelenka, 1992; Journée et al., 2012; Frei et al., 2015). Others use linear bias corrections (Polo et al., 2015), polynomial bias corrections (Mieslinger et al., 2014), or apply a polynomial to correct the satellite cumulative distribution function (Schumann et al., 2011). Ruiz-Arias et al. (2015) used optimal interpolation (OI) with numerical weather prediction solar radiation data and monthly-averaged daily GHI values from ground sensors.

OI is a Bayesian technique often used in geophysics, in particular numerical weather prediction, to combine models and observations. OI is mathematically equivalent to 3D variational methods, Kriging, and Gaussian process regression (Low et al., 2015). OI and 3D variational techniques are often used in the field of meteorology, Kriging is used in the context of geostatistics, and one often encounters Gaussian process regression in the context of machine learning. Thus, each method seeks a solution with the approach and quantities, like covariances, appropriate for each context.

In the context of this study, the satellite derived GHI estimates represent the model and the ground sensor data are the observations for OI. We focus on improvements to GHI estimates from a single satellite image using OI rather than improving the

* Corresponding author.

E-mail address: atlorenzo@email.arizona.edu (A.T. Lorenzo).

multi-year satellite estimates. This single satellite image will be used to nowcast DG production and to produce forecasts. We also present a novel method to parameterize the correlation between satellite pixels using the relative cloudiness between them.

We describe the satellite derived irradiance models and observation data in Section 2, the OI method in Section 3, and three ways to estimate covariances between locations in Section 4. These covariances are critical to the success or failure of OI. A method to correct for satellite geolocation errors is described in Section 5, and parameter tuning is detailed in Section 6. We present and discuss the results of applying OI to Tucson, AZ in Section 7. Finally, a summary of the work is provided in Section 8.

2. Models and observations

2.1. Satellite derived irradiance models

To investigate how well OI works with different types of prior information, we use two different models to convert satellite images to GHI maps. The resulting GHI maps are called the “background” or “prior” in OI and will be denoted by \mathbf{x}_b . Both models use images from the GOES-W geostationary satellite that cover the city of Tucson, AZ (roughly 75×80 km). An example of a visible albedo image derived from the visible channel of GOES-W is shown in Fig. 1.

One of the models is a physical model called the University of Arizona Solar Irradiance Based on Satellite (UASIBS) model (Kim et al., 2016). UASIBS uses the visible and infrared images from the GOES-W satellite to generate a cloud mask. Then, parameterized cloud properties determined from the infrared images are used in a radiative transfer model to determine the surface GHI. This GHI estimate has the same resolution as the visible channel of the GOES-W satellite (approximately 1 km).

The second model is a semi-empirical model, which we refer to as the SE model. This model is based on the SUNY model which applies a regression to the visible channel of the GOES-W satellite (Perez et al., 2002). The only differences between our SE model and the SUNY model are that the dynamic range is set with the 3 months of data used in this study instead of the recommended 60 day window with seasonal corrections and that the specular correction factor was neglected.

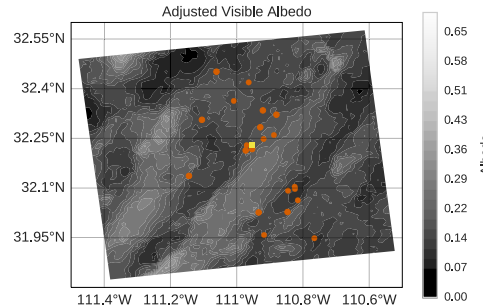


Fig. 1. Visible albedo image derived from the visible channel of the GOES-W satellite. Lighter colors indicate cloudier areas. The orange dots represent the locations of the sensors used in this study which includes both irradiance sensors and rooftop PV systems as described in Section 2.2. The yellow square in the center indicates the location of a calibrated GHI sensor on the University of Arizona campus. The image covers an area of roughly 75×80 km over Tucson, AZ. (For interpretation of the references to color in this figure legend, the reader is referred to the web version of this article.)

To remove effects of the diurnal cycle and ease incorporation of data from rooftop PV systems, all images were converted into clear-sky index images by dividing the estimated GHI by a clear-sky GHI estimate. The resulting values of clear-sky index range from nearly 0 for an overcast sky to 1 for a cloud-free sky. These conversion algorithms do not take into account image timestamp inaccuracies or satellite geolocation errors, but corrections for those errors will be discussed in Section 5.

2.2. Ground observations

The observation data are collected from 22 sensors including a calibrated NREL MIDC sensor (Wilcox and Andreas, 2010), custom irradiance sensors (Lorenzo et al., 2014), and data from rooftop PV systems. The sensor locations are indicated by orange circles in Fig. 1.

Irradiance observations were averaged to 5 min to match PV data that are reported as 5 min averages. This averaging is consistent with the inherent averaging due to the satellite spatial resolution. We note that all data sources (ground sensors and satellite images) are available in near real-time so that the OI corrected GHI images can be used as a basis for forecasts or DG nowcasts.

All data were converted to clear-sky index data using clear-sky expectations for each sensor. To produce the clear-sky expectation for one day, the measurements from preceding clear days within one week are averaged to produce an initial estimate. This initial estimate is then scaled to match the clear times on the day of interest to account for differences in turbidity or temperature. This method simplifies the calculation of clear-sky expectations for the rooftop PV systems because no parameters about the system (directional response, peak power) are assumed. The clear-sky expectations and clear-sky index data was inspected manually to confirm the quality. Note that the ground observation data may experience cloud enhancement events which lead to clear-sky indices greater than 1.

We restrict our data and analysis to solar zenith angles less than 60° . At times, we also withhold sensors from the OI routine and use these sensors to validate how well OI performs for other locations in the image besides the input sensor locations.

2.3. Data set description

About 1300 satellite images collected over April, May, and June 2014 were converted to irradiance images with the two models and paired with the corresponding ground observations. We randomly divide the data set into a training set with 437 images (252 clear and 185 cloudy images) and a verification set of 874 images (504 clear and 370 cloudy images). The training set is used to tune parameters for OI as described in Section 6. The verification set is used for error analysis and to draw conclusions about OI.

The distinction between clear and cloudy satellite images will become important in Section 3 for determining sensor error variances. Clear times are identified using a combination of the UASIBS estimates and the ground sensor data. Specifically, if the minimum value of a UASIBS clear-sky index image is greater than 0.8, the mean of the image is greater than 0.99, and the second largest deviation from 1 of any of the ground observations is less than 0.05, then we classify the image as clear. This procedure accurately identifies times at which no clouds exist in the area of study. Other methods can also be used to perform this classification (Reno and Hansen, 2016; Escrig et al., 2013; Ghonima et al., 2012), but our simple method is sufficient for our purposes.

3. Optimal interpolation

We now describe the OI method. Under wide assumptions, OI is optimal in the sense that it is the best linear, unbiased estimator of a field. Further detail can be found in data assimilation textbooks, e.g. Kalnay (2003).

The result of the OI routine, known as the analysis, \mathbf{x}_a , is a vector that is produced by computing a weighted sum of the background (or prior information), \mathbf{x}_b , and a correction vector (or “innovation” in OI) that depends on the measurements, \mathbf{y} :

$$\mathbf{x}_a = \mathbf{x}_b + \mathbf{W}(\mathbf{y} - \mathbf{H}\mathbf{x}_b). \quad (1)$$

As discussed in Section 2.1, the N satellite derived clear-sky indices from one image are represented as the background vector, \mathbf{x}_b . The measurement vector, \mathbf{y} , is a vector of length M of clear-sky indices generated from M ground irradiance sensor and rooftop PV power data observations as discussed in Section 2.2. The observation matrix, \mathbf{H} , is an $M \times N$ matrix that maps points in the background space to points in the observation space. We construct \mathbf{H} using the nearest neighbor approach of selecting the satellite pixels that are closest to the observation locations. Another possible approach is to average the points in the background that are within a given radius of each sensor location. Furthermore, \mathbf{H} can contain conversion factors to convert the units of \mathbf{x}_b to the units of \mathbf{y} . In our case however, \mathbf{H} is unitless because \mathbf{y} and \mathbf{x}_b are both in units of clear-sky index. Example background and analysis images for the UASIBS and SE models are shown in Fig. 2.

The weight matrix, \mathbf{W} , is an $N \times M$ matrix constructed from the error covariance matrices of the background, \mathbf{P} , and the observations, \mathbf{R} , as

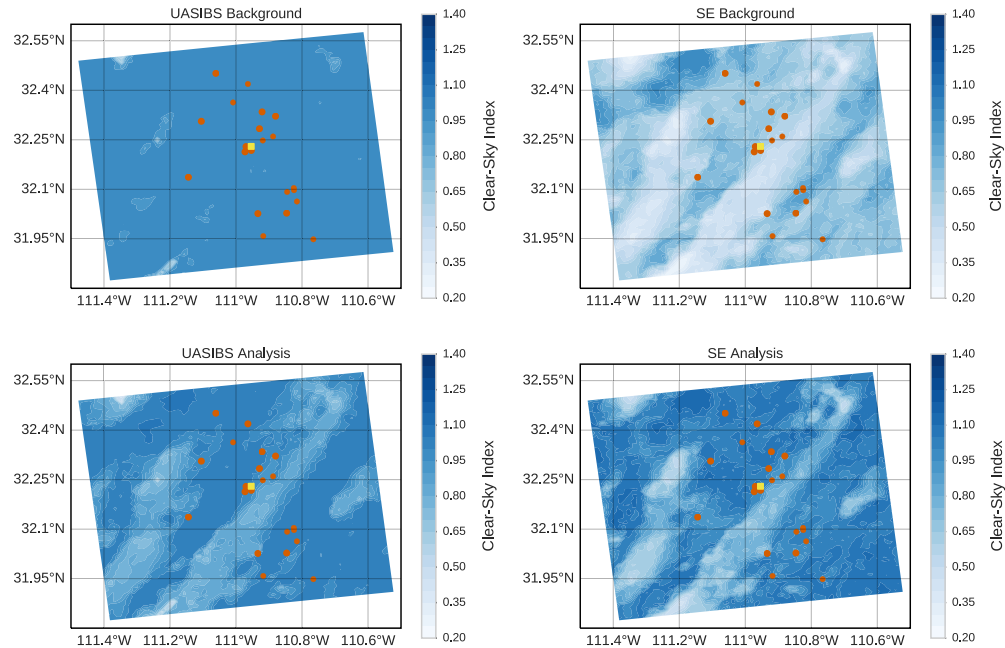


Fig. 2. Example background (top row) and analysis (bottom row) clear-sky index images using the UASIBS (left column) and SE (right column) satellite image to ground irradiance models applied to the visible satellite image shown in Fig. 1. Note that in this case, UASIBS failed to produce many clouds. OI adds clouds to the analysis and also makes the darker, clear areas even more clear. In this case, the SE model overproduces clouds. OI reduces the cloud amount while keeping clouds in suitable locations.

$$\mathbf{W} = \mathbf{PH}^T(\mathbf{R} + \mathbf{PHP}^T)^{-1}. \quad (2)$$

Choosing these error covariance matrices must be done with care: they define how information is transferred from sensor locations to other locations in the satellite image, and how much weight is given to any one sensor or satellite pixel.

\mathbf{R} is defined as the error covariance matrix of the observations such that

$$\mathbf{y} = \mathbf{y}_t + \mathbf{e}, \quad \mathbf{e} \sim N(\mathbf{0}, \mathbf{R}) \quad (3)$$

where \mathbf{y}_t is the true value of the observation and \mathbf{e} is a random vector sampled from a multivariate normal distribution with mean 0 and covariance \mathbf{R} . On clear days, we assume the true clear-sky index values are 1.0. We also assume that the measurements are unbiased and that the correlations in the errors between sensors is negligible, so \mathbf{R} is a diagonal matrix in our case. Thus, we estimate the diagonal elements (sensor error variances) by computing the variance on a set of clear days in the training data set for each sensor individually. Furthermore, we restrict the minimum variance to be 0.001 or about a 3% clear-sky index RMS error to avoid exact interpolation at sensor locations. With \mathbf{R} calculated from the ground sensor data, we describe various ways to parameterize \mathbf{P} next.

4. Covariance parameterization and correlation structure

Choosing an appropriate background error covariance matrix is an important step in the OI method for this application and determines how well OI performs. The background error covariance matrix, \mathbf{P} , defines how information is transferred from sensor

observation locations to locations throughout the background image. Similar to \mathbf{R} , \mathbf{P} is defined such that

$$\mathbf{x}_b = \mathbf{x}_t + \mathbf{g}, \quad \mathbf{g} \sim N(\mathbf{0}, \mathbf{P}) \quad (4)$$

where \mathbf{x}_t is the “true” value of the satellite derived clear-sky index image and \mathbf{g} is a random vector sampled from a multivariate normal distribution with mean 0 and covariance \mathbf{P} .

We will now describe three methods to calculate \mathbf{P} :

1. *Empirical*: \mathbf{P} calculated empirically from all of the background images,
2. *Spatial*: \mathbf{P} with correlations parameterized based on the physical distance between pixels, and
3. *Cloudiness*: \mathbf{P} with correlations parameterized based on the difference in cloudiness between each pixel.

4.1. Empirical covariance

The empirical \mathbf{P} is calculated by assuming that satellite-derived clear-sky index images are sampled from the same multivariate normal distribution and then simply computing the covariance using all images in the training data set. This assumption is likely invalid given the high probability of clear days leading to a non-Gaussian distribution. An analysis computed with this type of \mathbf{P} gives non-physical results, as described in Section 7, but is included for comparison.

4.2. Correlation matrix parameterization

Before describing spatial and cloudiness covariances, it is useful to decompose \mathbf{P} into a diagonal variance matrix, \mathbf{D} , and a correlation matrix, \mathbf{C} as

$$\mathbf{P} = \mathbf{D}^{1/2} \mathbf{C} \mathbf{D}^{1/2}. \quad (5)$$

Here, \mathbf{D} sets the scale of the errors while \mathbf{C} describes how errors and information spread. We obtain \mathbf{D} in a similar manner as we do for \mathbf{R} , we use a number of clear images from the training data set to estimate the variance of each pixel in the background individually. The errors in \mathbf{x}_b come mainly from the satellite image to ground irradiance conversion that often exhibits large differences in error between clear and cloudy images. Thus, we allow for a tunable scaling factor, d , in the construction of \mathbf{D} for cloudy images to account for possible model error differences between clear and cloudy skies so that

$$\mathbf{D} = d\mathbf{D}' \quad (6)$$

where \mathbf{D}' is the variance estimated from the clear images.

The correlation matrix \mathbf{C} defines how information is transferred from the sensor locations to other locations in the satellite estimate. \mathbf{C} can be parameterized based on the spatial distance between points in the background as in Ruiz-Arias et al. (2015) or, as we demonstrate, one might rely on information in the current satellite image, such as cloudiness.

To construct the elements of \mathbf{C} , c_{ij} , we apply a correlation function, k , to the distance metric r computed between each pixel i and j

$$c_{ij} = k(r_{ij}). \quad (7)$$

Any number of covariance functions, k , can be chosen; see Rasmussen and Williams (2005) for a partial list. We chose to study a piece-wise linear correlation function

$$k(r) = \begin{cases} 1 - \frac{r}{l} & r < l \\ 0 & r \geq l \end{cases} \quad (8)$$

an exponential correlation function

$$k(r) = \exp\left(-\frac{r}{l}\right), \quad (9)$$

and a square exponential correlation function

$$k(r) = \exp\left(-\frac{r^2}{l^2}\right). \quad (10)$$

For each correlation function, l is a characteristic length that we tune with a training data set for each choice of k to minimize error as described later in Section 6.

4.3. Spatial covariance

The distance metric for the spatial correlation parameterization is the standard Euclidean distance (once locations are mapped to a two dimensional plane using a map projection),

$$r_{ij} = \sqrt{(x_i - x_j)^2 + (y_i - y_j)^2}. \quad (11)$$

Thus, the spatial covariance \mathbf{P} is constructed by applying Eqs. (5)–(7) and (11) with a tuned k , l , and d as described in Section 6.

4.4. Cloudiness covariance

For what we call cloudiness covariance, we parameterize \mathbf{C} based on the difference in cloudiness in the visible satellite image. This corresponds to only adjusting the cloudy areas with observations that are experiencing similarly cloudy sky and leaving the clear areas to be adjusted by observations of the clear sky. This adjustment is made without consideration of the spatial distance between pixels. We use the adjusted visible albedo calculated from the visible satellite image rather than the processed clear-sky index maps to compute the correlation. This avoids cloud representation errors that may arise in the satellite to irradiance conversion; for example, note how UASIBS fails to produce clouds in many areas of Fig. 2. Also note that because this parameterization depends on the visible satellite image, \mathbf{C} and subsequently \mathbf{P} are calculated for each image individually.

To calculate the adjusted visible albedo, we convert the visible brightness counts from the satellite, b_i , to visible albedo and divide by the cosine of the solar zenith angle, ϕ , to correct for the time of day:

$$v_i = \left(\frac{b_i}{255}\right)^2 / \cos(\phi_i). \quad (12)$$

An example of this adjusted visible albedo is shown in Fig. 1. We also remove the constant (over the three months we studied) background albedo that is due to the land surface. This background is calculated as the average of the adjusted visible albedo on clear days in the training set so that

$$z_i = v_i - \bar{v}_i^{\text{clear}} \quad (13)$$

The distance metric for the cloudiness correlation parameterization is the absolute value of the difference between pixel values of the adjusted visible albedo image (with the land surface background removed):

$$r_{ij} = |z_i - z_j|. \quad (14)$$

Thus, the cloudiness covariance \mathbf{P} is constructed by applying Eqs. (5)–(7) and (12)–(14) with a tuned k , l , and d for each individual satellite image.

4.5. OI summary

In summary, to perform OI, one must first collect background, \mathbf{x}_b , and observation, \mathbf{y} , data. Then define observation error covari-

ances, \mathbf{R} , from the observation data and define the background error covariances, \mathbf{P} , either empirically or by following the above procedure after choosing a distance metric r , the correlation function k , the correlation length l , and the scaling factor d using Eqs. (5)–(7). Finally, Eqs. (1) and (2) can be used to compute the analysis, \mathbf{x}_a .

5. Geolocation correction

It is important to consider errors in the tagged location for each satellite pixel compared to the ground sensors and the time-stamp of the image. Furthermore, one must take into account the position of the sun in order to predict the cloud shadow location on the ground. If this cloud shadow location is inaccurate, the optimal interpolation routine may perform poorly, or worse, may invert the cloudy and clear areas of the images. Examples of an inverted analysis and the corrected analysis once these position adjustments are taken into account are shown in Fig. 3.

The first geolocation issue is called parallax, which is the discrepancy between the actual location and the location tagged by a satellite due to the satellite viewing the scene at an angle (Vicente et al., 2010). The GOES-W satellite is located at 135°W on the equator while Tucson, AZ is at roughly 32°N and 110°W. The satellite tags the location of each pixel as if it were at the surface. This means, for our region, that a cloud obscures a pixel that is to the NE of the cloud. Thus, the actual location of the cloud is to the SW of what the satellite tags the pixel as.

Another source of error is a timing issue that arises because the satellite tags each image with a single time, however it may take

the satellite 30 min to sweep and capture that image. Thus, there is uncertainty in the time that any part of the image was captured.

Estimating where the cloud shadow falls on the surface due to solar position effects is the final geolocation issue we take into account. If the shape and height of the clouds is known, the correction for both parallax and solar position is a simple geometry problem. However, cloud shape and height are difficult to determine with sufficient accuracy, and we rely only on an estimate of the height of the top of the clouds and ignore the vertical thickness. We also assume that the cloud height is uniform in one image.

Given these limitations, we use a simple strategy to correct for geolocation errors. We find a single optimal cloud height by minimizing the mean squared error (MSE) between the OI analysis and sensors that are not used to perform OI. The sensors not used are the same cross-validation sensors we will discuss next. We perform this correction using a grid search for cloud heights ranging from 0 to 14 km and we shift the entire background image based on that height, perform OI, then calculate the MSE. Once the height that minimizes MSE is found, we perform OI again on the shifted background image and save the analysis as our result for the given time. This technique assumes that there is a single cloud layer, which is not always the case and can be improved in the future.

6. Tuning OI to a specific location

As discussed in Section 4.2, k , l , and d are tunable parameters that determine how information is spread through the image. In order to find suitable values of these parameters, we split the satellite images into a training and a verification set as described

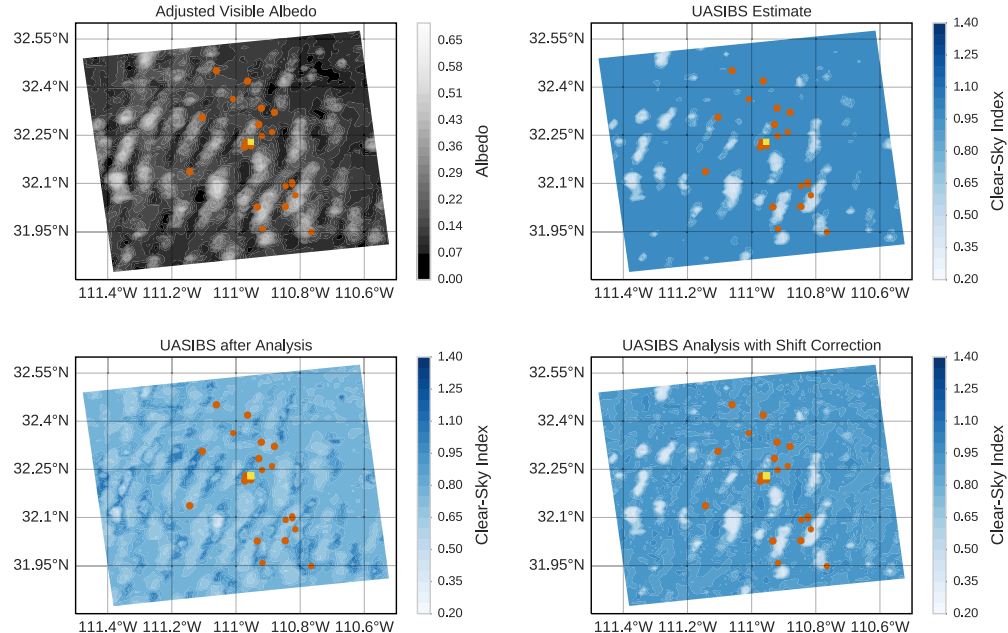


Fig. 3. An example of a time when errors in geolocation of the satellite image result in an analysis that is inconsistent with the actual satellite image. The background estimate in this case (upper right) agrees well with the visible satellite image (upper left). However, after performing OI, the analysis (lower left) has clouds in areas that should be clear according to the visible image and sometimes makes areas that should have clouds clear. After shifting the background image slightly, OI produces an analysis (lower right) that is consistent with the visible image.

in Section 2.3, and tuning is only performed with the training set. Furthermore, we perform a six fold cross-validation over the sensors in order to validate the model at locations not included in the OI calculation. We then perform a grid search through the parameter space and define the optimal parameters as those that give the lowest mean (over the cross-validation sets) MSE of the withheld sensors. This tuning is performed for both spatial and

cloudiness correlation parameterizations and for both the SE and UASIBS models.

The optimal parameters for the UASIBS and SE models using both cloudiness and spatial covariances computed only using the training data are presented in Table 1. We note that these parameters are optimal for Tucson, AZ. Other areas, sensors, or study periods may require a different parameterization of the error covariances.

Table 1

Optimal parameters for the UASIBS and SE models for both cloudiness and spatial covariances. l has units of adjusted visible albedo for cloudiness covariances and units of kilometers for spatial covariances.

		d	l	k
UASIBS	Cloudiness	156	0.2	Linear
	Spatial	225	20	Exp.
SE	Cloudiness	1.56	0.6	Exp.
	Spatial	0.25	100	Exp.

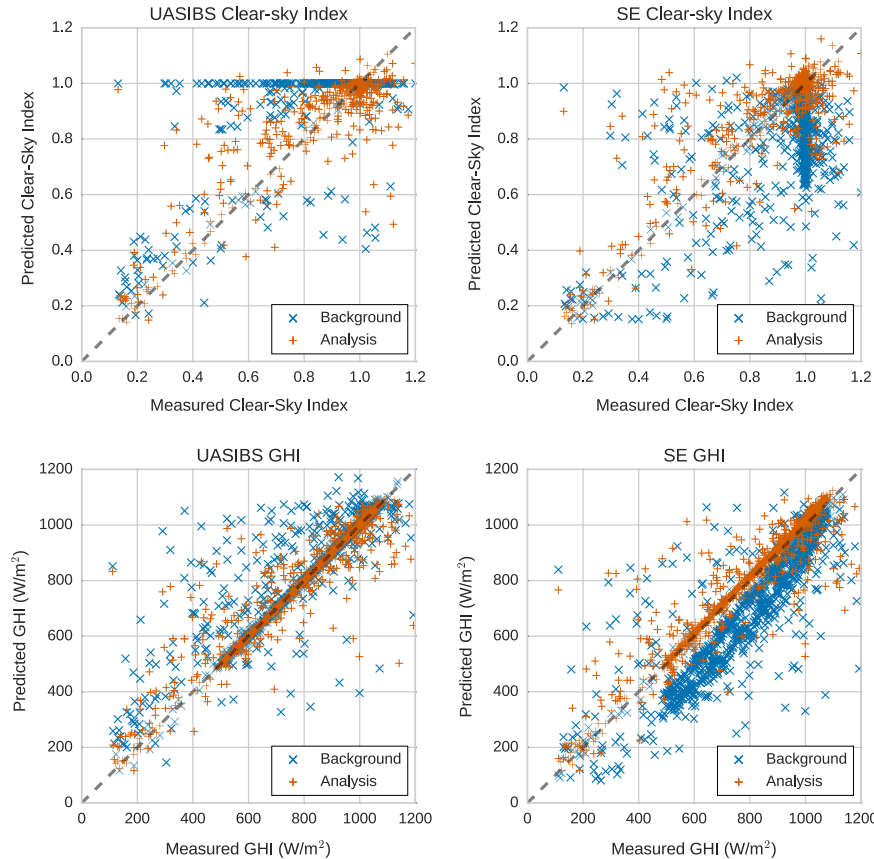


Fig. 4. Scatter plots of predicted versus measured clear-sky index (top row) and GHI (bottom row) for the calibrated NREL MIDC GHI sensor on the University of Arizona campus for both the UASIBS model (left column) and SE model (right column). The analysis was computed using cloudiness covariance, the optimal parameters listed in Table 1, and the verification data set. Data from the background images is plotted as blue 'x's and data from the OI analysis is plotted as orange '+'s. GHI is computed by multiplying clear-sky indices and an appropriate clear-sky profile. In each case, we see that the analysis values are more tightly scattered around the dashed $y = x$ line. Also notice that the UASIBS model does not predict clear-sky index values from roughly 0.6 to 0.8 but that the analysis does move some values into this range. (For interpretation of the references to color in this figure legend, the reader is referred to the web version of this article.)

In general, the minimum MSE is sensitive to the parameter choice with the most sensitivity shown for l and least sensitivity for k . A small change in l (0.1 for cloudiness and 10 km for spatial) typically degrades the MSE by 10% or more. One exception is the combination of the SE model and spatial covariance which produce MSE surfaces that are less sensitive to a range of parameters, for example a 40 km difference in l only raises the MSE by 10%.

Large d values for the UASIBS model indicate that the estimated variance from only the clear days is too low. This is because UASIBS suppresses many clouds or slight variations on clear days. An example of this on a cloudy day is shown in Fig. 2. A value of $d < 1$ for the SE model indicates that the model tends to overestimate the variance on cloudy days as a result of the tendency to overproduce clouds even at times that should be clear.

Our proposed tuning process is computationally intensive but manageable; computation for one set of (k, l, d) and one cross-validation set using 24 cores of two Intel Xeon E5-2690 v3 processors takes nearly 10 min. Thus, to tune over the six cross-validation sets, three choices of k , ten choices of both l and d , spatial and cloudiness correlation parameterizations, and the SE and UASIBS models would take nearly 7 weeks on a single 24 core machine. It would take a typical 4 core laptop or desktop nearly a year to perform the same tuning. To speed up this tuning, the bulk of the operations were converted to GPU code which decreased the run-time for a single parameter set over the test data to 5 min using a single GPU. We used the University of Arizona's El Gato supercomputer, which has 140 NVIDIA K20x GPUs, to perform the tuning in a matter of days. Once tuning is complete, OI can be computed in under five seconds for each image.

7. Results and discussion

We compute the OI analysis on each of the images in the verification data set using optimal parameters found in Section 6. First, we compute the analysis of the verification data by only withholding the NREL MIDC GHI sensor at the University of Arizona, and later we calculate errors while performing six fold cross-validation over the sensors.

Scatter plots of predicted versus measured values at the NREL MIDC sensor using cloudiness covariance are shown in Fig. 4. In the clear-sky index scatter plots, we see that the UASIBS model under-predicts clouds while the SE model over-predicts clouds. It is interesting to note that the UASIBS model does not predict clear-sky index values between 0.6 and 0.8, and that OI helps to fill in this gap. The GHI scatter plots show that the analysis performs well and is more tightly scattered around the $y = x$ line with minimal bias. It is especially striking to note how well OI improves the GHI estimates for the SE model. Figs. 2 and 4 also demonstrate that OI is not simply a bias correction applied to the whole background because the analysis is not a linear (or even polynomial) function applied to the background values. This is especially evident in the scatter plot of GHI for the SE model (lower right of Fig. 4).

We compute the mean bias error (MBE), mean absolute error (MAE), and root mean squared error (RMSE) over the verification data with 5 min average sensor data and "instantaneous" satellite estimates. For RMSE, the square root is computed after all averaging computations. The errors in GHI when only the NREL MIDC sensor was withheld from the OI routine and converting clear-sky index to GHI using the sensor's clear-sky profile are shown in Table 2.

To calculate the errors over the cross-validation sensors in order to validate OI at locations not included in the algorithm, we averaged over the withheld sensors, the cross-validation runs, and the verification images. Fig. 5 shows the reduction in errors for the UASIBS and SE models using cloudiness covariance for the analysis

Table 2

Error statistics for the NREL MIDC sensor on the University of Arizona campus. The analysis was computed with only the MIDC sensor withheld and averaged over the verification data set, and cloudiness covariance was used. Both the UASIBS and SE models show improvements and have a similar analysis RMSE. Units are W/m^2 .

	MBE	MAE	RMSE
UASIBS analysis	4.16	27.2	71.1
UASIBS background	20.7	38.8	98.8
SE analysis	11.2	36.0	72.7
SE background	-86.1	107	140

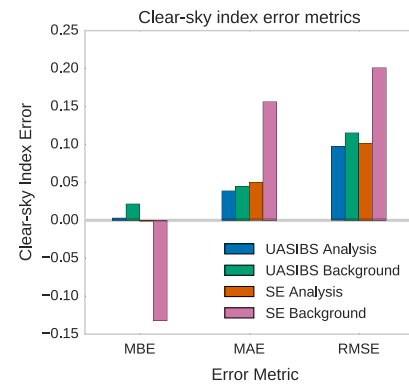


Fig. 5. Clear-sky index cross-validation error statistics for the UASIBS and SE models before (background) and after (analysis) performing OI using cloudiness covariance with the optimal parameters listed in Table 1. The error statistics were computed by averaging over the withheld sensors, the cross-validation runs, and the verification times. The SE model initially has a large bias that is corrected by the analysis. After analysis, both the UASIBS and SE models have similar RMSE.

errors as compared to the background errors. Table 3 presents the errors for the background and analysis computed with each covariance method for the UASIBS and SE models, respectively. Analyzing Figs. 4 and 5 and Tables 2 and 3, we see that the SE model initially has a large bias that is corrected in the analysis. This also leads to large MAE and RMSE relative improvements of 68% and 50%, respectively. The analysis using the best covariance parameterization for UASIBS had a RMSE relative improvement of 16%.

Furthermore, it is interesting to see that the errors after optimal interpolation are similar for both the UASIBS and SE models. We interpret this as evidence that one can use the relatively simple

Table 3

Clear-sky index error statistics using the UASIBS and SE models with cloudiness, spatial, or empirical covariance parameterizations. Errors are calculated by averaging over the withheld sensors, cross-validation runs, and verification images. OI using any of the covariance methods improves upon the background for both models. All errors are in units of clear-sky index.

	MBE	MAE	RMSE
<i>UASIBS model</i>			
Cloudiness analysis	0.003	0.039	0.097
Spatial analysis	0.004	0.038	0.099
Empirical analysis	0.000	0.043	0.105
Background	0.022	0.045	0.115
<i>SE model</i>			
Cloudiness analysis	-0.001	0.050	0.102
Spatial analysis	-0.005	0.051	0.105
Empirical analysis	-0.001	0.051	0.106
Background	-0.132	0.156	0.201

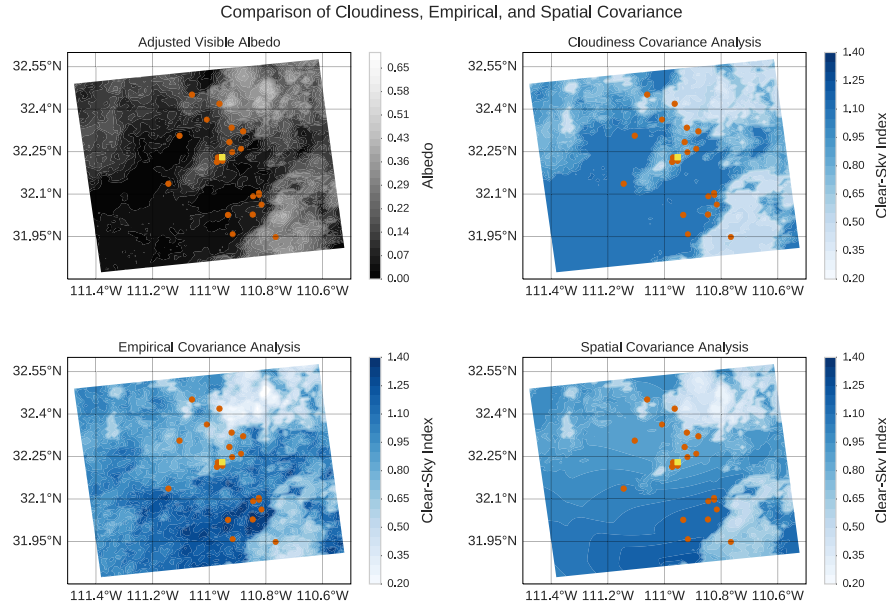


Fig. 6. Example of OI using empirical, spatial, and cloudiness covariance with the UASIBS model. The upper left shows the visible image taken from the satellite with the surface albedo removed. The upper right shows the analysis using cloudiness covariance that generally agrees with the visible albedo image. The analysis computed with an empirical covariance matrix (bottom left) generates clouds in the lower left of the image that are not present in the visible albedo image. The spatial covariance analysis (bottom right) shows a smoothly varying and thin “background cloud” that is inconsistent with the visible albedo image.

semi-empirical model with optimal interpolation and still obtain irradiance estimates that are comparable in quality to estimates from more complicated, physics-based models. This also suggests that the optimal interpolation routine that we have presented is likely to work with satellite image to irradiance models that were not studied here.

OI assumes that the background error is unbiased and Gaussian as described in Eq. (4). However, it is clear from Fig. 5 that the SE background is biased. From Fig. 4, it also appears that the UASIBS background is not Gaussian. Thus, we cannot assume that this application of OI yielded the best linear unbiased estimate, but we show that OI still produces measurable improvements.

The results in Table 3 indicate that any of the three methods to compute the background error covariance matrix produce an analysis that improves upon the background. However, when we subjectively compare the analysis of the covariance models, as in Fig. 6, we see that analysis using the cloudiness covariance method better represents the cloud pattern depicted in the visible satellite image. Clouds produced using the spatial and empirical covariance methods are physically inconsistent with the clouds depicted in the visible albedo image. For example, the lower left corner of the images in Fig. 6 should have no clouds present according to the visible albedo image, but the empirical covariance analysis has clouds present in that region. The analysis produced using spatial covariance shows a thin and smoothly varying “background cloud” that is simply not observed in the visible albedo image. Furthermore, the cloudiness covariance parameterization is calculated for each satellite image individually which likely leads to a better modeling of the spatial heterogeneity of irradiance. Thus, we recommend the cloudiness covariance parameterization as the method of choice, but additional verification sensors evenly dis-

tributed throughout the study area may help to better distinguish the parameterizations through objective measures.

8. Conclusions

We presented an application of optimal interpolation that combines ground irradiance sensor data with a satellite derived estimate of irradiance. We systematically analyzed three methods to choose an error covariance matrix for the satellite derived GHI estimates. This covariance matrix is critical to the success of OI. We observed the best results by assigning covariances based on the differences in cloudiness rather than spatial or empirical covariances. Our implementation of OI was trained and evaluated using three months of data in Tucson, AZ. We tuned the model parameters over one-third of the data, and presented the results of OI over the remaining two-thirds.

The results show that OI improves the entire satellite derived irradiance field with data from only a small number of point locations. Furthermore, the success of OI with different satellite derived irradiance models indicates that OI is likely applicable to satellite derived irradiance models not described in this paper.

In future work, we wish to study if OI is applicable to larger areas than the city scale studied here. If, for example, clouds form because of the same physical forcings, OI using cloudiness covariance may be able to use sensors in Tucson to improve irradiance estimates 100 miles away in Phoenix. Furthermore, OI as described in this paper can be extended to a Kalman filter with the use of a cloud advection model. This allows forecasts to be made that also incorporate previous satellite and ground sensor data instead of relying on a single snapshot in time.

Conflict of interest

The authors have no conflicts of interest to report.

Supplementary material

Location metadata, measurements, clear-sky expectations, and the satellite data used in this study have been released online under the CC0 1.0 license (Lorenzo and Cronin, 2016). The code to generate the optimal interpolation analysis is released under the MIT license (Lorenzo, 2016).

Acknowledgments

This project was funded in part by Tucson Electric Power and Arizona Public Service. We thank Technicians for Sustainability, a local solar PV installer, for providing data from rooftop PV systems. ATL thanks the University of Arizona Renewable Energy Network for support. WFH thanks the Department of Energy (DOE) Office of Energy Efficiency and Renewable Energy (EERE) Postdoctoral Research Award for support. This material is based upon work performed on the El Gato supercomputer supported by the National Science Foundation under Grant No. 1228509. This material is based upon work supported by the National Science Foundation under Grant No. 1619630.

References

- D'Agostino, V., Zelenka, A., 1992. Supplementing solar radiation network data by co-Kriging with satellite images. *Int. J. Climatol.* 12 (7), 749–761. <http://dx.doi.org/10.1002/joc.3370120707>.
- Drews, A., de Keizer, A., Beyer, H., Lorenz, E., Betscke, J., van Sark, W., Heydenreich, W., Wiemken, E., Stettler, S., Toggweiler, P., Bofinger, S., Schneider, M., Heilscher, G., Heinemann, D., 2007. Monitoring and remote failure detection of grid-connected PV systems based on satellite observations. *Sol. Energy* 81 (4), 548–564. <http://dx.doi.org/10.1016/j.solener.2006.06.019>.
- Escrí, H., Battlés, F., Alonso, J., Baena, F., Bosch, J., Salbidegoitia, I., Burgaleta, J., 2013. Cloud detection, classification and motion estimation using geostationary satellite imagery for cloud cover forecast. *Energy* 55, 853–859. <http://dx.doi.org/10.1016/j.energy.2013.01.054>.
- Frei, C., Willi, M., Stöckli, R., Dürr, B., 2015. Spatial analysis of sunshine duration in complex terrain by non-contemporaneous combination of station and satellite data. *Int. J. Climatol.* 35 (15), 4771–4790. <http://dx.doi.org/10.1002/joc.4322>.
- Ghonima, M.S., Urquhart, B., Chow, C.W., Shields, J.E., Cazorla, A., Kleissl, J., 2012. A method for cloud detection and opacity classification based on ground based sky imagery. *Atmos. Meas. Tech.* 5 (11), 2881–2892. <http://dx.doi.org/10.5194/amt-5-2881-2012>.
- Journéa, M., Müller, R., Bertrand, C., 2012. Solar resource assessment in the Benelux by merging Meteosat-derived climate data and ground measurements. *Sol. Energy* 86 (12), 3561–3574. <http://dx.doi.org/10.1016/j.solener.2012.06.023>.
- Kalnay, E., 2003. *Atmospheric Modeling, Data Assimilation and Predictability*. Cambridge University Press.
- Kim, C.K., Holmgren, W.F., Stovern, M., Betterton, E.A., 2016. Toward improved solar irradiance forecasts: derivation of downwelling surface shortwave radiation in arizona from satellite. *Pure Appl. Geophys.* <http://dx.doi.org/10.1007/s00024-016-1302-3>.
- Kühnert, J., Lorenz, E., Heinemann, D., 2013. Satellite-based irradiance and power forecasting for the German energy market. In: Kleissl, J. (Ed.), *Solar Energy Forecasting and Resource Assessment*. Elsevier, pp. 267–297. <http://dx.doi.org/10.1016/B978-0-12-397177-7.00011-5> (Chapter 11).
- Lorenzo, A.T., 2016. alorenzo175/satellite_irradiance_optimal_interpolation: Final Research Code. <http://dx.doi.org/10.5281/zenodo.166799>.
- Lorenzo, A.T., Cronin, A.D., 2016. Irradiance Measurements, Satellite Images, and Clear-sky Expectations for Spring 2014 in Tucson, AZ. <http://dx.doi.org/10.5281/zenodo.166799>.
- Lorenzo, A.T., Holmgren, W.F., Leuthold, M., Kim, C.K., Cronin, A.D., Betterton, E.A., 2014. Short-term PV power forecasts based on a real-time irradiance monitoring network. In: 2014 IEEE 40th Photovoltaic Specialist Conference (PVSC), pp. 0075–0079. <http://dx.doi.org/10.1109/PVSC.2014.6925212>.
- Low, K.H., Chen, J., Hoang, T.N., Xu, N., Jailllet, P., 2015. Recent Advances in Scaling Up Gaussian Process Predictive Models for Large Spatiotemporal Data. Springer International Publishing, pp. 167–181. http://dx.doi.org/10.1007/978-3-319-25138-7_16.
- Mieslinger, T., Ament, F., Chhatbar, K., Meyer, R., 2014. A new method for fusion of measured and model-derived solar radiation time-series. *Energy Procedia* 48, 1617–1626. <http://dx.doi.org/10.1016/j.egypro.2014.02.182>.
- Perez, R., Ineichen, P., Moore, K., Kmiecik, M., Chain, C., George, R., Vignola, F., 2002. A new operational model for satellite-derived irradiances: description and validation. *Sol. Energy* 73 (5), 307–317. [http://dx.doi.org/10.1016/S0038-092X\(02\)00122-6](http://dx.doi.org/10.1016/S0038-092X(02)00122-6).
- Polo, J., Martin, L., Vindel, J., 2015. Correcting satellite derived DNI with systematic and seasonal deviations: application to India. *Renew. Energy* 80, 238–243. <http://dx.doi.org/10.1016/j.renene.2015.02.031>.
- Polo, J., Wilbert, S., Ruiz-Arias, J., Meyer, R., Gueymard, C., Suri, M., Martin, L., Mieslinger, T., Blanc, P., Grant, I., Boland, J., Ineichen, P., Remund, J., Escobar, R., Troccoli, A., Sengupta, M., Nielsen, K., Renne, D., Geuder, N., Cebeaucer, T., 2016. Preliminary survey on site-adaptation techniques for satellite-derived and reanalysis solar radiation datasets. *Sol. Energy* 132, 25–37. <http://dx.doi.org/10.1016/j.solener.2016.03.001>.
- Rasmussen, C., Williams, C., 2005. Covariance functions. In: *Gaussian Processes for Machine Learning*. MIT Press, pp. 79–104 (Chapter 4).
- Reno, M.J., Hansen, C.W., 2016. Identification of periods of clear sky irradiance in time series of GHI measurements. *Renew. Energy* 90, 520–531. <http://dx.doi.org/10.1016/j.renene.2015.12.031>.
- Ruiz-Arias, J.A., Quesada-Ruiz, S., Fernández, E.F., Gueymard, C.A., 2015. Optimal combination of gridded and ground-observed solar radiation data for regional solar resource assessment. *Sol. Energy* 112, 411–424. <http://dx.doi.org/10.1016/j.solener.2014.12.011>.
- Saint-Drenan, Y.-M., Bofinger, S., Rohrig, K., Ernst, B., 2011. Regional nowcasting of the solar power production with PV-plant measurements and satellite images. In: Proceedings of the ISES Solar World Congress 2011. International Solar Energy Society, Freiburg, Germany, pp. 1–11. <http://dx.doi.org/10.18086/swc.2011.11.09>.
- Schumann, C., Beyer, H.G., Meyer, R., Chhatbar, K., 2011. Improving satellite-derived solar resource analysis with parallel ground-based measurements. In: Proceedings of the ISES Solar World Congress 2011. International Solar Energy Society, Freiburg, Germany, pp. 1–12. <http://dx.doi.org/10.18086/swc.2011.24.28>.
- Vicente, G.A., Davenport, J.C., Scofield, R.A., 2010. The role of orographic and parallax corrections on real time high resolution satellite rainfall rate distribution. *Int. J. Remote Sens.* 32 (2), 221–230. <http://dx.doi.org/10.1080/01433160010006935>.
- Vignola, F.E., McMahan, A.C., Grover, C.N., 2013. Bankable solar-radiation datasets. In: Kleissl, J. (Ed.), *Solar Energy Forecasting and Resource Assessment*. Elsevier, pp. 97–131. <http://dx.doi.org/10.1016/B978-0-12-397177-7.00005-X> (Chapter 5).
- Wilcox, S., Andreas, A., 2010. Solar Resource & Meteorological Assessment Project (SOLRMAP): Observed Atmospheric and Solar Information System (OASIS), Tucson, Arizona (Data). <http://dx.doi.org/10.7799/105226>.

APPENDIX C

LIST OF PUBLICATIONS CO-AUTHORED BY A. T. LORENZO

Peer-reviewed publications:

1. goes here

Presentations and posters:

1. poster

Other works:

1. other stuff

REFERENCES

- [1] GTM Research/SEIA, “U.S. Solar Market Insight Q4 2016: Executive Summary,” GTM Research, SEIA, Tech. Rep., 2016. [Online]. Available: <https://www.greentechmedia.com/research/subscription/u.s.-solar-market-insight>
- [2] P. L. Joskow, “Comparing the Costs of Intermittent and Dispatchable Electricity Generating Technologies,” *American Economic Review*, vol. 101, no. 3, pp. 238–241, may 2011. [Online]. Available: <http://dx.doi.org/10.1257/aer.101.3.238>
- [3] J. Kleissl, Ed., *Solar Energy Forecasting and Resource Assessment*, 1st ed. Oxford: Elsevier, 2013. [Online]. Available: <http://dx.doi.org/10.1016/B978-0-12-397177-7.18001-5>
- [4] R. H. Inman, H. T. Pedro, and C. F. Coimbra, “Solar forecasting methods for renewable energy integration,” *Progress in Energy and Combustion Science*, vol. 39, no. 6, pp. 535–576, dec 2013. [Online]. Available: <http://dx.doi.org/10.1016/j.pecs.2013.06.002>
- [5] D. Cormode, “Large and Small Photovoltaic Powerplants,” PhD Dissertation, University of Arizona, 2015.